Biochemistry **2003,** *42,* 4357−4372

Hydrogen Bonds in Rubredoxins from Mesophilic and Hyperthermophilic Organisms[†]

Catherine M. Bougault,[‡] Marly K. Eidsness,[§] and James H. Prestegard*[,‡]

Complex Carbohydrate Research Center and Department of Chemistry, University of Georgia, Athens, Georgia 30602

Received December 2, 2002; Revised Manuscript Received February 17, 2003

ABSTRACT: The extent and strength of the hydrogen bond networks in rubredoxins from the hyperthermophile *Pyrococcus furiosus* (PfRd), and its mesophilic analogue *Clostridium pasteurianum* (CpRd), are examined and compared using NMR spectroscopy. NMR parameters examined in this study include through-hydrogen bond $^{h3}J_{NC'}$ scalar couplings and ^{1}H, ^{13}C, and ^{15}N chemical shifts, as well as covalent $^1J_{NH}$ and $^1J_{NC'}$ scalar couplings. These parameters have allowed the characterization in solution of 12 hydrogen bonds in each protein. Despite a 83% sequence homology and a low RMSD for the backbone heavy atoms (0.648 Å) in the crystalline state, subtle, but definite, changes have been identified in the detailed hydrogen-bonding patterns. CpRd shows an increased number of hydrogen bonds in the triple-stranded β-sheet and an additional hydrogen bond in the multiple-turn segment including residues 14−32. On the other hand, PfRd exhibits an overall strengthening of N−H···O═C hydrogen bonds in the loops involved at the metal binding site as well as evidence for an additional NH···S(Cys) hydrogen bond involving the alanine residue 44. These data, as well as temperature dependence of the NMR parameters, suggest that the particular NMR hydrogen bond pattern found in the hyperthermophile rubredoxin leads to an increased stabilization at the metal binding pocket. It seems to result from a subtle redistribution of hydrogen-bonding interactions between the triple-stranded β-sheet and the actual metal binding site.

Hyperthermophile organisms have received increased attention in the past 20 years due to both their practical and fundamental significance. On the practical side, highly thermostable enzymes, either natural or engineered, represent a great potential for biochemical and industrial applications (*1*). On the fundamental side, comparison of extremophilic proteins and their mesophilic counterparts provides a unique perspective for understanding the molecular and physical basis to protein stability (*2* and references cited therein). To date, careful statistical examinations of structural and sequence information on nonredundant families of thermophilic and mesophilic proteins have, however, failed to unambiguously point to explanations for the observed differences in protein stabilities (*3*−*5*). The analyses, in fact, suggest the need for additional experimental data that can speak more directly to energetic contributions at specific sites in the proteins. In this context, the present study examines rubredoxins from a mesophile, *Clostridium pasteurianum*, and a hyperthermophile, *Pyrococcus furiosus*, using recently developed techniques in NMR spectroscopy, among them those that allow observation of scalar couplings across hydrogen bonds. Emphasis is, therefore, on hydrogen bond strengths and their possible implications for thermostability.

Among the 70 hyperthermophilic species described until 2001, rubredoxin has been purified from only one archaeon, *P. furiosus* (Pf)[1] (*6*). This anaerobic organism, first isolated by Fiala and Stetter (*7*) in 1986 from marine sulfataric fields in Italian volcanic areas, achieves optimal growth at 100 °C, pH 7.0, in 2% NaCl. Like most enzymes isolated and characterized in Pf, rubredoxin (PfRd) has proved to be remarkably thermostable, remaining unaffected after incubation at 95 °C for 24 h (*8*). Three mesophilic counterparts to PfRd have been extensively described and characterized in the literature: *Desulfovibrio gigas* [DgRd, 68% primary sequence identity (si) and 78% primary sequence homology (sh) (*9*)], *Desulfovibrio vulgaris* [DvRd, 72% si/82% sh (*10*)], and *C. pasteurianum* rubredoxins [CpRd, 57% si/83% sh (*11*)] (*12*). Kinetic stability of mesophilic proteins has been reported to be significantly less than that of PfRd (*13*): a 25% decrease of the visible absorption was observed after 1 h at 80 °C in the case of DgRd (*14*), and a 50% decrease was observed after 5.8 h at 92 °C, pH 7.8, in the case of

---

[†] This work was supported by Grant MCB 9726341 from the National Science Foundation (to C.M.B. and J.H.P.) and by a CRCT grant from the University Joseph Fourier, Grenoble, France (to C.M.B.).

* To whom correspondence should be addressed. Phone: (706) 542-6281. Fax: (706) 542-4412. E-mail: jpresteg@ccrc.uga.edu.

[‡] Complex Carbohydrate Research Center, University of Georgia.

[§] Department of Chemistry, University of Georgia.

[1] Abbreviations: Pf, *Pyrococcus furiosus*; Cp, *Clostridium pasteurianum*; Dv, *Desulfovibrio vulgaris*; Dg, *Desulfovibrio gigas*; Rd, rubredoxin; IPTG, isopropyl β-D-thiogalactopyranoside; fMet-PfRdZn, N-terminal formylmethionine form of *P. furiosus* zinc rubredoxin; Met-PfRdZn, N-terminal methionine form of *P. furiosus* zinc rubredoxin; wt-PfRdZn, wild-type recombinant form of *P. furiosus* zinc rubredoxin lacking the N-terminal methionine; fMet-CpRdZn, N-terminal formylmethionine form of *C. pasteurianum* zinc rubredoxin; Met-CpRdZn, N-terminal methionine form of *C. pasteurianum* zinc rubredoxin; si, sequence identity; sh, sequence homology; HSQC, heteronuclear single-quantum coherence; NOE, nuclear Overhauser effect; IPAP, in-phase/antiphase.

10.1021/bi027264d CCC: $25.00

CpRd (*15*). Cavagnero et al. (*16*) have confirmed these results by measuring the unfolding rate constants of CpRd (350 s^{-1}) and PfRd (2.3 s^{-1}) at pH 2.0, a nonphysiological but necessary condition to bring unfolding into an experimentally acceptable time scale. Thermodynamic stability on the contrary has been more difficult to assess. The irreversible nature of the unfolding of rubredoxins has in fact prevented the use of calorimetric analyses. Nevertheless, a minimal free energy of stabilization of 63 kcal/mol at 100 °C and an extrapolated melting temperature of 176−195 °C have been proposed for PfRd on the basis of hydrogen exchange kinetics studied as a function of temperature (*17*). For a comparison, a denaturation temperature of 83 °C has been reported for CpRd in a recent study (*18*).

In addition to the quantification of thermodynamic and kinetic parameters, a number of studies have focused on dissecting the individual contributions to thermostability. Monitoring the unfolding of PfRd by absorption spectroscopy, tryptophan fluorescence emission, and far-UV circular dichroism, Cavagnero et al. (*19*) have proposed a low-pH unfolding mechanism of four steps: a partial release of secondary structural elements, loss of the iron atom that is coordinated to the protein through cysteinyl sulfurs of two consensus cysteine motifs, CXXC and CPXC, a subsequent denaturation of the characteristic three-stranded antiparallel β-sheet "zipping" the N-terminal to the C-terminal end of the protein, and relaxation of the hydrophobic core. The same authors (*19*) and others (*18*) have shown that despite a high structural homology, characterized by a 0.47 Å RMS deviation in the C_α atomic positions (*20*) and the conservation of all secondary elements, CpRd follows a very different pathway. Metal coordination, hydrophobicity, salt bridges, and hydrogen bonds are nevertheless involved in the unfolding process, making these interactions potential molecular determinants of PfRd's exceptional thermostability.

While there have been few systematic studies of these possible determinants, there is a good deal of relevant data; we attempt to review that here. Metal chelating loops defined by residues 5−11 and 38−44 are highly conserved in all rubredoxins. In each of the centers defined by X-ray crystallography (*11*, *20*) the $Fe(S\text{-}Cys)_4$ site and the peptide backbone atoms of the loops exhibit a pseudo-2-fold symmetry. The centers include six NH···S(Cys) interactions, two for each of the buried ligands, C6 and C39, and one for each of the cysteines located at the surface of the protein, C9 and C42. In solution, five of these hydrogen bonds have been unambiguously identified by NMR through $N^1H\cdots S(Cys)-{}^{113}Cd$ scalar couplings in ^{113}Cd-substituted PfRd (*21*, *22*). No similar observations have been reported for CpRd, although the same hydrogen bond network is expected for CpRd in solution. In principle, failure to detect hydrogen bonds by similar methods in CpRd could provide evidence for stronger hydrogen bonds in PfRd, but hydrogen-bonding distances are known to be shorter in the Cd-substituted protein than in the native protein, making the interpretation of such results difficult (*23*).

The van der Waals interactions also may be important. Such interactions have been proposed between I8 β-H, I41 β-H, A44 β-CH_3, and C6, C39, C42 sulfur atoms to explain correlations detected in a HSED $^1H-{}^{199}Hg$ NMR experiments collected on ^{199}Hg-substituted PfRd (*24*). As these residues are mutated into V8, L41, and V44 in CpRd, fine structural differences may affect solvent accessibility to the side chains of metal ligands C9 and C42 and hence affect thermostability of metal binding. No direct data on CpRd have been reported to our knowledge. Nevertheless, V44A mutation in CpRd has led to a conformational change implying a shorter NH···S(Cys) hydrogen bond (*25*, *26*). Differences in the metal chelate loops are thus clearly modulating the stability of the native $Fe(S\text{-}Cys)_4$ site, although it may not be the key determinant to PfRd thermostability and appears to not even be required for folding. In fact, Strop and Mayo (*27*) have engineered a PfRd mutant that folded in the absence of metal and that exhibited a reversible unfolding at 82 °C. More recently, Zartler et al. (*28*) have shown that similar phenomena may be observed in apoproteins. PfRd appears to retain a good deal of native structure in the absence of metal. In contrast, CpRd apoprotein adopts a structure distinctly different from that of its holo form at room temperature and completely unfolds at approximately 40 °C.

Compactness and hydrophobicity of hyperthermophiles and mesophiles have been compared and declared essentially identical (*4*). Furthermore, mutation of the PfRd hydrophobic core to match that of CpRd showed no change in the thermostability of the metal-free apoproteins (*28*). Nonpolar side chains of residues I8, I12, I24, and L52 and to a lesser extent residues V5, L33, W37, and V38 are exposed to the surface in PfRd (*29*). Tight van der Waals contacts between these hydrophobic residues have been proposed to reinforce the stability of secondary structure elements and to diminish destabilizing interactions with the solvent. In particular, molecular dynamics simulations on site-directed PfRd mutants have shown that the V5/I12/L52 cluster aggregates tightly and stabilizes the β-sheet (*30*). Nevertheless, thermostability studies on CpRd and PfRd chimera have suggested that this contribution is small. In fact, mutation of CpRd residues 1−15 and 48−54 into the corresponding PfRd residues only has a moderate impact on the stabilization of rubredoxin (*15*).

PfRd is the only rubredoxin that normally lacks an N-terminal methionine residue. Electrostatic interactions between the alanine N-terminal amino group and a glutamate carboxylic side chain (E15) have been proposed to prevent the "unzipping" of the β-sheet secondary structure at elevated temperature (*8*, *31*). However, the thermostability decrease resulting from the elimination of this interaction was shown to be only moderate through comparison of different PfRds (*32*) or comparison of metal-free PfRdXC4 (*27*) N-terminal variants. Additional salt bridges in PfRd versus CpRd have been mentioned, especially between lysine side-chain amino groups (K7, K46, and K29) and glutamate or aspartate carboxylic side chains (E50, E31 or D35, E32, respectively). The thermostability study by Cavagnero et al. (*13*, *16*) at pH = 2, where these interactions are absent, nevertheless argues against a major role in the mechanism of PfRd stabilization.

Hydrogen bonds have also been proposed as potential contributors to PfRd thermostability. In addition to an extension of the β-sheet hydrogen bond network toward the N-terminal alanine (E15→A2 CO, L52→K3), PfRd has been ascribed a unique set of interactions between the E15 carboxylic side chain, the W4 imidazolyl proton, and the F30 amide proton (*31*). While attempts to reproduce this hydrogen bond network in CpRd by introducing specific mutations [M1(−)/A2K/P15E triple mutation] failed (*33*), more extensive substitution in a chimera containing the first two strands of the CpRd β-sheet combined with the last 39 residues of PfRd has been shown to be kinetically more destabilized than native CpRd (*15*). However, these mutation results are difficult to interpret, and a more thorough and direct investigation of hydrogen-bonding contributions seems warranted.

Recently, NMR experiments have been described that detect individual partners of hydrogen bond pairs (*34*, *35*). Using scalar couplings between hydrogen bond donor and hydrogen bond acceptor nuclei, a range of hydrogen-bonding interactions has been directly observed in proteins, including backbone amide/backbone carbonyl (*36*−*40*), backbone amide/side-chain carboxylate (Asp, Glu) (*41*, *42*), side-chain amino group (Arg)/side-chain carboxylate (Asp, Glu) (*43*), and side-chain histidine/side-chain histidine interactions (*44*). In addition, the size of the scalar coupling ${}^{h3}J_{NC'}$ has been shown to provide quantitative information on the geometry, and then the strength, of the considered hydrogen bonds. In fact, an empirical exponential dependence of ${}^{h3}J_{NC'}$ on the N···O distance has been established (*42*, *45*), which has been supported by quantum chemical calculations (*46*−*48*) and extended to include HCO and HCON angular dependence (*46*, *49*, *50*). To date, through-hydrogen bond scalar couplings have been shown to be one of the most sensitive parameters in proteins to characterize subtle structural rearrangements upon temperature (*51*), pressure (*52*), ligand binding (*53*), and helix formation of peptides (*54*).

Taking advantage of these recent NMR developments, in conjunction with NMR parameters such as chemical shifts and one-bond ${}^{1}J_{NH}$, ${}^{1}J_{NC'}$ scalar couplings, we investigate in the present study the extent and strength of the hydrogen bond network in both Cp and Pf rubredoxins in solution.

EXPERIMENTAL PROCEDURES[2]

Protein Sample Preparation and Characterization. [U-^{15}N,^{13}C]-CpRdZn and PfRdZn were overexpressed in *Escherichia coli* strain BL21(DE3) (Novagen, Inc.) and purified according to previously published procedures (*15*). For the production of these uniformly labeled samples, Luria−Bertani medium was replaced by an M9 minimal medium supplemented with 1 g/L $^{15}NH_4Cl$, 4 g/L uniformly labeled [^{13}C]glucose, 1 mM $MgSO_4$ and 100 μM $CaCl_2$. Zinc sulfate (25 mg/L) was added instead of iron salts after induction with IPTG to yield the zinc-substituted rubredoxins. Two samples containing respectively 2.2 mM [U-^{15}N,^{13}C]-CpRdZn, 50 mM potassium phosphate buffer, and 200 mM NaCl in H_2O/D_2O (9/1), pH = 6.25, and 4.7 mM [U-^{15}N,^{13}C]-PfRdZn, 50 mM potassium phosphate buffer, and 200 mM NaCl in H_2O/D_2O (9/1), pH = 6.44, were prepared for NMR experiments. pH values were measured using a Aldrich glass/calomel combined microelectrode, and reported values were uncorrected for D_2O isotopic effects (*55*).

When expressed in *E. coli*, PfRdZn is actually produced as a mixture of three forms, the N-terminal formyl-Met (fMet-PfRdZn), the N-terminal-Met (Met-PfRdZn), and the “wild-type” (wt-PfRdZn) forms. Although these forms exhibit a slight difference in terms of thermostability (*32*), it is small in comparison to stability issues of Pf versus Cp. As a consequence, the three forms were not separated. Integration of peak volumes in a protein purification chromatogram suggested the following composition for the mixture: 74.5% fMet-PfRdZn, 10.9% Met-PfRdZn, and 14.6% wt-PfRdZn, which is in reasonable agreement with ^{15}N-HSQC NMR data (70%/15%/15%, respectively, after volume measurement on a few resolved NHs in the [^{1}H,^{15}N]-HSQC). Previous X-ray and NMR studies reported Cp rubredoxin as a single N-terminal methionine form. Nevertheless, the assignment procedure, mainly through the HNCO experiment, suggested that a major portion (∼75% from volume integration in the [^{1}H,^{15}N]-HSQC and HNCO spectra) of the [U-^{15}N,^{13}C]-recombinant protein is actually produced as an N-terminal formylmethionine form. The presence of the different forms of rubredoxins, as well as the uniform labeling, was confirmed in the CpRdZn and PfrdZn samples by electrospray ionization mass spectrometry (*56*).

Resonance Assignment. All NMR spectra were recorded on Varian Inova systems operating at 600 or 800 MHz proton frequency. Each spectrometer was equipped with a 5 mm triple-resonance HCN probe with axial gradient capabilities.

A restricted set of experiments was collected at 25 °C to assign the backbone for each of the two samples: 2D [^{1}H,^{15}N]-HSQC (*57*), 3D HNCO, and 3D HNCACB experiments (*58*) using sequences in the manufacturer-supplied ProteinPack (Varian Inc.) pulse program library. A modified version of 3D HCACO (*59*) was recorded to provide resonance assignments for carbonyl carbons in residues positioned directly before prolines in the sequence. This experiment included a SCUBA scheme during the presaturation period employed for water suppression in order to recover magnetization from the resonances close to or under the water. Previous backbone assignments established through HNCO and HNCACB experiments could also be clearly confirmed with this pulse sequence. Backbone chemical shift assignment was completed with the extraction of proline ^{15}N chemical shifts from a 2D version of the HCA(CO)N triple-resonance experiment (*60*), conducted after D_2O exchange on each sample. For all of these sequences, quadrature detection in the indirectly detected dimension was obtained by the States−TPPI (*61*) or by the echo/antiecho method (*62*).

A 3D [^{1}H,^{1}H,^{15}N]-TOCSY-HSQC was collected with a 60 ms mixing time to extract each residue spin system. Further aliphatic ^{1}H/^{13}C assignments were performed on the basis of a 3D H(C)CH-TOCSY experiment with gradient selection (*63*). Tyr and partial Phe aromatic side-chain ^{1}H resonances were assigned using a combination of (HB)CB-(CGCD)HD and (HB)CB(CGCDCE)HE experiments (*64*). 2D versions of [^{1}H,^{1}H,^{13}C]-HSQC-TOCSY with a 200 ms mixing time and [^{1}H,^{1}H,^{13}C]-HSQC-NOESY with 200 and 500 ms mixing times including WET water suppression then provided the missing ^{1}H aromatic side-chain resonances (*65*). Corresponding ^{13}C resonances were obtained using a sensitivity-enhanced [^{1}H,^{13}C]-HSQC with a gradient coherence

---

[2] In the Results and Experimental Procedures, hydrogen bonds are noted from the donor (usually a backbone amide N−H) to the acceptor (usually a backbone carbonyl group) with arrows. Cp and Pf rubredoxins sequences have been aligned, and residue numbering according to CpRd has been adopted. This results in a shift of one residue in wild-type Pf protein, which lacks the N-terminal methionine.

selection step (*57*). Aromatic quaternary $^{13}C_\gamma$ resonances were assigned on the basis of the HCBCG pulse scheme published by Löhr and Rüterjans (*66*). A 3D version of the gHCACO experiment adapted for the observation of side-chain correlations (*67*) allowed the detection and assignment in D_2O of side-chain carboxyl carbon nuclei from Asp and Glu residues through single carbon−carbon scalar connectivities. Experimental details of each experiment including sweep width and time/frequency domain matrix sizes are given as Supporting Information (Table S1).

The NMR data sets were processed with Felix 2000 (Accelrys Inc.). Data processing typically consisted of solvent suppression using a time domain sine-bell convolution function in the direct dimension, a forward−backward linear prediction in the indirect dimension, multiplication of the FID by a Kaiser window function in all dimensions, zero filling to the final matrix size, and Fourier transformation. As initial values of the incremented delays in multidimensional experiments were set so as to allow a predictable phasing in each dimension and minimimum roll of the baseline, no baseline correction was performed on any of the data sets.

All ^1H dimensions were referenced to internal DSS (2,2-dimethyl-2-silapentane-5-sulfonate sodium salt) at 0.00 ppm. ^{13}C and ^{15}N dimensions were indirectly referenced to DSS as previously described (*68*). Complete assignments for both CpRdZn and PfRdZn have been deposited at the BioMagResBank, University of Wisconsin−Madison, WI, under the Accession Numbers 5518 and 5971, respectively (*69*).

Chemical Shift Temperature Dependence. Gradient sensitivity-enhanced [^1H,^{15}N]-HSQCs and 2D versions of the HNCO experiments were collected every 10 °C over the temperature range 10−70 °C for CpRdZn and 10−80 °C for PfRdZn. Data acquisition and processing parameters are identical to those described in the previous section. Temperature was calibrated against 100% methanol in the temperature range 0−45 °C and against 100% ethylene glycol in the temperature range 35−90 °C (*70*). ^1H_N chemical shifts were referenced against DSS at each temperature, and $^{13}C'$ and ^{15}N chemical shifts were indirectly referenced accordingly. Peak picking was performed using Felix 2000 tools. Temperature gradients $\Delta\delta/\Delta T$ (in ppb/K) were derived after a linear least-squares fit of the chemical shift as a function of temperature.

Chemical shift deviations (CSD, in ppm) were calculated as the difference between the observed chemical shift at 20 °C and the corresponding random coil value at the same temperature. Random coil chemical shifts were taken from the Schwarzinger et al. data set (*71*), and corrections for local sequence effects (taking into account the nature of residue $i - 2$, $i - 1$, $i + 1$, $i + 2$) were included (*72*). Ring current shifts for ^1H nuclei were calculated using the program Shifts 4.1 from Case et al. (*73*) and the crystal structures of higher resolution (PDB code 1irn for CpRd and PDB code 1bq9 for PfRd) (*74*).

Cross-Hydrogen Bond Scalar Couplings ($^{h3}J_{NC'}$, $^{h2}J_{HC'}$). Hydrogen-bonding partners were first identified using the long-range HNCO experiment described by Cordier and Grzesiek (*36*). Different modifications of this sequence [S^3 HNCO-TROSY (*39*), CPD-HNCO (*41*)] resulted in enhanced sensitivities but left the number of detected hydrogen bonds unchanged in each protein. Quantification of the through-hydrogen bond scalar couplings, $^{h3}J_{NC'}$, at 25 °C was performed with the quantitative *J*-correlation long-range HNCO experiment described by Cordier and Grzesiek (*36*) and the S^3 HNCO-TROSY experiment described by Meissner and Sørensen (*39*). Experiments were performed at 600 or 800 MHz for both proteins. Typical 2D reference and through-H-bond correlation spectra were recorded with 96 complex increments and 53 ms acquisition time in the t_1 dimension and 1024 complex points and 114 ms acquisition time in the t_2 dimension. After optimization, the $^{15}N-^{13}C'$ de/rephasing constant time delay (T) was set to 65.5 ms for optimal suppression of residual one-bond couplings, corresponding to the average $^1J_{NC'}$ value of 15.2−15.3 Hz in both rubredoxins. A delay (ζ) of 16.6 ms was used in the constant time period between the ^{15}N and $^{13}C'$ refocusing pulses in the reference experiment. Total experimental times were 55 and 6 h for each cross-hydrogen and reference experiment, respectively. Matrices (2048 × 2048) were generated within Felix 2000 using processing parameters identical to those previously described. Peak volumes were measured within this software.

Absolute $^{h3}J_{NC'}$ values were calculated, after extraction of $^1J_{NC'}$ from measurements described in the following section, using the relation (*36*)

$$\sin(2\pi{}^{h3}J_{NC'}T)/\cos[2\pi{}^{h3}J_{NC'}(T-\zeta)] = \sqrt{I_{cross}n_{ref}/I_{ref}n_{cross}}\,\sin[2\pi{}^{1}J_{NC'}(T-\zeta)]/\cos(2\pi{}^{1}J_{NC'}T) \quad (1)$$

where I_{cross} and I_{ref} are the peak volumes, respectively, from the cross and reference spectra and n_{cross} and n_{ref} refer respectively to the number of transients used for data collection in the cross and reference experiments. A grid search algorithm was used to extract the through-hydrogen bond coupling constants. Estimated coupling constant errors based on the signal-to-noise ratio of the individual experiments yielded an error of 0.5 Hz for the $^1J_{NC'}$ coupling constant values, and standard error propagation analysis produced errors in the range of 0.02−0.05 Hz for $^{h3}J_{NC'}$ couplings. Experimental determination of the sign of $^{h3}J_{NC'}$ scalar couplings was not considered, and values are reported as negative according to Cornilescu et al. (*42*). Dependence of $^{h3}J_{NC'}$ values on temperature was determined using only the quantitative *J*-correlation long-range HNCO experiment at 10, 25, and 40 °C for CpRdZn and at 10, 25, 40, and 50 °C for PfRdZn. In the temperature study, $^{h3}J_{NC'}$ coupling constants were not corrected for the $^1J_{NC'}$ scalar coupling, and the approximate relation $^{h3}J_{NC'} = [1/(2\pi T)](I_{cross}n_{ref}/I_{ref}n_{cross})^{1/2}$ was used.

$^1J_{NH}$ and $^1J_{NC'}$ Scalar Couplings. Different experimental approaches have been described in the literature for the precise measurements of one-bond N−H scalar couplings, where splittings are measured either in the frequency domain or through resonance intensity in two subspectra. In the present study, three independent data sets have been collected for each protein: a ^1H-coupled [^{15}N,^1H]-HSQC experiment (*75*) including gradient coherence selection for sensitivity enhancement, an IPAP [^1H,^{15}N]-HSQC (*76*), and a phase-encoded [^1H,^{15}N]-HSQC (*77*). Spectra were recorded at 25 °C with sweep widths of 8956.6 and 2500 Hz in ^1H and ^{15}N dimensions, respectively, on an Inova 600 spectrometer.

Experimental data sets consisted of 2K data points in the direct dimension and 256 or 128 data points in the indirect dimension for the frequency- or intensity-based experiments, respectively. A constant time period of 0.215 ms was used in the phase-encoded [^{1}H,^{15}N]-HSQC. Residual solvent was removed by convolution difference, and data were apodized with a Kaiser window function prior to Fourier transformation. Zero filling was performed to produce 2048 × 2048 (alternatively 2048 × 512) matrices containing the left half (amide region) of the 2D spectrum. A total of 16 transients per increment yielded a signal-to-noise ratio of 40:1 for ^{1}H-coupled spectra. Splittings in the frequency domain were measured directly on the 2D spectra using a peak-picking algorithm with quadratic interpolation and on 1D slices in the ^{15}N dimension using a Gaussian line-fitting algorithm. Both routines are available in the Felix 2000 package (Accelrys Inc.). Volumes in the two subspectra [sine and cosine modulated signals (*77*)] generated from the phase-encoded [^{1}H,^{15}N]-HSQC were measured in Felix 2000, and coupling constants were extracted accordingly. $^1J_{NH}$ scalar coupling values collected in these experiments were all in agreement within 0.5 Hz.

A ^{13}C′-coupled [^{1}H,^{15}N]-HSQC experiment, including gradient coherence selection for sensitivity enhancement, was collected for the determination of $^1J_{NC'}$ scalar coupling constants on each protein sample. Data consisted of 1024 complex points in the direct dimension and 256 complex points in the indirect dimension with sweep widths of 8956.6 and 2240 Hz, respectively. A total of 64 transients per increment yielded a signal-to-noise ratio greater than 100:1. Spectra were processed to generate 2048 × 4096 matrices. Scalar coupling values were measured according to the same procedure described above for $^1J_{NH}$ coupling constants in the frequency-based approach. The values obtained were used in the computation of through-hydrogen bond coupling constants. Three series of measurements showed that values are reproducible within a standard error of 0.2 Hz.

Experimental determination of the signs of $^1J_{NC'}$ and $^1J_{NH}$ scalar couplings was not pursued, but values are reported as negative, considering the negative sign of the nitrogen gyromagnetic ratio. Scalar coupling constants are provided as Supporting Information (Table S4) and have been deposited at the BioMagResBank, University of Wisconsin—Madison, WI, with assignments for CpRdZn and PfRdZn, respectively.

RESULTS

Resonance Assignments and Methionine Processing. The observation of electron-mediated scalar couplings between nuclei on both sides of a hydrogen bond using a long-range HNCO allows the identification of hydrogen bond partners and yields quantitative information on the bond geometry. Resonance assignment of the hydrogen bond donor (amide proton) and the hydrogen bond acceptor (carbonyl carbon) is nevertheless a prerequisite to such analysis. Partial resonance assignments have been reported in the literature for various forms of Cp and Pf rubredoxins [Zn, Fe^{II} (*78*, *79*), Fe^{III} (*80*)], including in particular all amide protons of the diamagnetic zinc forms (*33*, *81*). With adequate amide chemical shift dispersion, assignments could in principle be extended to ^{15}N and ^{13}C′ using the HNCO experiments. However, three to five of the correlations detected in the long-range HNCO for each of the proteins show a carbon chemical shift corresponding to a carbonyl resonance that could not be identified in this simple approach. Candidates for the corresponding assignments include backbone carbonyls of residues preceding prolines or carboxyl/carbonyl groups from side chains of Glu, Gln, Asp, or Asn residues, neither of which would show connectivity to backbone ^{15}N−^{1}H resonances. However, problems could also arise from undetected or incorrectly assigned ^{15}N−^{1}H correlations. Therefore, an independent complete assignment procedure was undertaken.

Backbone carbonyl carbons were tackled first, applying the same procedure for both rubredoxins. ^{1}H, ^{15}N, ^{13}C$_\alpha$, and ^{13}C$_\beta$ resonances were assigned sequentially in fragments using HNCACB 3D spectra. Glycine, threonine, and alanine unique carbon chemical shifts were used for sequence-specific identification of the fragments separated by proline residues (five in total for each rubredoxin). A 3D HNCO completed most of the backbone assignments by adding carbonyl chemical shifts. Two cross-peaks at unusual carbon chemical shifts, between 166 and 168 ppm, were noted. A [^{1}H,^{13}C]-HSQC spectrum showed that these correlations arise from a single carbon with a $^1J_{CH} = 198$ Hz scalar coupling to an isolated proton at 8.14 and 8.19 ppm for CpRdZn and PfRdZn, respectively. These features are attributed to the presence of a formyl group that remains covalently linked to the N-terminal methionine as a result of incomplete processing of overexpressed rubredoxins by the deformylase and methionyl aminopeptidase of *E. coli* (*32* and SWISS-PROT reports). Furthermore, two (respectively three) sets of resonances are detected for some residues in the HNCO and the [^{1}H,^{15}N]-HSQC spectra of CpRdZn (respectively PfRdZn), which is consistent with the presence in the NMR sample of the *N*-formylmethionine (fMet-CpRdZn, 75%) and the *N*-methionine (Met-CpRdZn, 25%) forms in the case of CpRd [respectively *N*-formylmethionine (fMet-PfRdZn, 70%), the *N*-methionine (Met-PfRdZn, 15%), and the wild-type (wt-PfRdZn, 15%) in the case of PfRd]. Volume integration revealed in both cases the predominance of the *N*-formylmethionine form in the double-labeled samples studied in this work.

Using the [^{1}H,^{1}H,^{15}N]-HSQC-TOCSY, all ^{1}H$_\alpha$ and most ^{1}H$_\beta$ were assigned. Missing backbone carbonyl resonances, particularly from residues preceding prolines, could then be extracted from a 3D HCACO experiment with the exception of N25 in CpRdZn (due to overlap of the H$_\alpha$ chemical shift with water). This experiment was also analyzed to confirm the so far obtained sequential assignments. Rubredoxin backbone assignments were completed by adding proline nitrogen chemical shifts using a 2D version of a HCA(CO)N experiment collected in D_2O. Despite completion of the backbone assignments, only one additional hydrogen bond acceptor could be identified in the long-range PfRdZn HNCO spectrum: A44. The assignment procedure consequently had to be extended to protein carboxylic/amide side chains.

For aliphatic side chains, ^{1}H and ^{13}C assignments were completed on the basis of a 3D gradient sensitivity-enhanced HCCH-TOCSY experiment in H_2O (*63*). Focus was directed toward unambiguous Asp and Asn H$_\beta$/C$_\beta$, as well as Glu and Gln H$_\gamma$/C$_\gamma$, assignments as a route to side-chain carboxyl and carbonyl carbon identification. Connectivities to the last

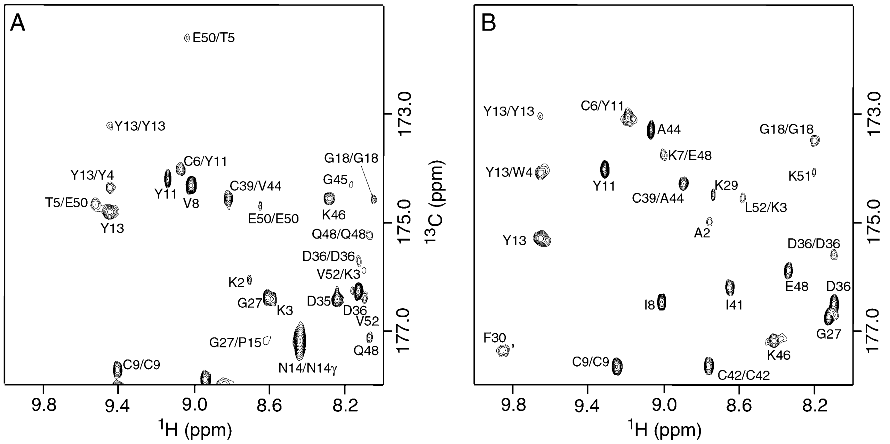

FIGURE 1: Section of the S^3 HNCO-TROSY (*39*) collected at 25 °C on an Inova 600 spectrometer for CpRd (A) and PfRd (B) samples. Through-hydrogen bond correlations ($^{h3}J_{NC'}$) are marked by the residue number of the amide group followed by the residue number of the carbonyl acceptor. Two- ($^{2}J_{NC'}$) and three- ($^{3}J_{NC'}$) bond intraresidue connectivities are marked by the residue number of the amide group and the residue number of the carbonyl or carboxylic carbon. Residual one-bond ($^{1}J_{NC'}$) connectivities are marked by the residue number of the corresponding amide group.

nuclei were established with the same strategy as that used for the backbone carbonyl carbon assignments, i.e., through a modified HCACO sequence. The resolution in the quaternary carbon dimension was enough to distinguish and assign all of the peaks on a 2D spectrum. During t_1 evolution, the ^{13}C carrier was shifted to 182 ppm, and a shaped pulse centered on 37 ppm was used to decouple the aliphatic carbons (*67*). Using this scheme, all side-chain carbonyl groups could be assigned with the exception of the PfRd E15 carboxylic group. Data collection in D$_2$O and the COCAH sequence proposed by Dijkstra et al. (*82*) gave no further improvement with respect to detection of this resonance.

At this stage, all carbon frequencies detected in the long-range HNCO could be identified and are reported in Figure 1. Nevertheless, aromatic side-chain assignments were pursued in order to complete the protein NMR characterizations. A combination of HBCBCG (*66*), (HB)CB(CGCD)-HD, (HB)CB(CGCDCE)HE (*64*), [^{1}H,^{13}C]-HSQC, 2D [^{1}H,^{13}C]-HSQC-TOCSY, and [^{1}H,^{13}C]-HSQC-NOESY (*57*) was pursued for that purpose, yielding a total of 635 (97.2%) and 635 (96.9%) magnetically distinguishable nuclei assigned for the *N*-formyl-Met predominant form of CpRd and PfRd, respectively. The unassigned resonances remaining include nitrogen atoms of lysine side chains, some aromatic quaternary carbons, the PfRd E15 carboxylic carbon, and highly exchangeable protons such as Tyr, Thr, and Ser OHs or Lys NH$_2$s.

The other forms of rubredoxins were assigned to a lesser extent due to their lower abundance in the mixture (25% of Met-CpRdZn and 15% each of Met-PfRdZn and wt-PfRdZn). Backbone-only chemical shifts were extracted from the HNCACB, [^{1}H,^{15}N]-HSQC, and 3D HNCO experiments. It has to be noted that, in the case of PfRd, nuclei could be assigned to particular residues but not unambiguously to each of the individual minor forms (Met-PfRd and wt-PfRd) of the protein due to signal overlap with the major species. Resulting ^{1}H$_N$, ^{15}N, and ^{13}C′ chemical shift standard deviations between fMet-CpRdZn and Met-CprdZn, as well as between fMet-PfRdZn, Met-PfrdZn, and wt-PfRdZn, are depicted in Figure 2. In the case of Cp rubredoxin, chemical shift changes are located in the first (residues 1−5) and last (residues 50−52, 54) strands of the triple-stranded β-sheet, which suggests a localized conformational change of the protein backbone upon formylation. It also induces a perturbation of residues 28−32 that are structured in a 3$_{10}$-helix and, most particularly, the amide proton of F30 and the nitrogen and carbonyl carbon of K31. Adjustment of the hydrophobic interactions between F30 and Y4 might be invoked to explain the observed cooperative effect. In PfRd additional perturbations are observed in the turn region going from residue 13 to residue 18, and a discrete change can be noted for residue K46. Again, the hydrogen-bonding interac-

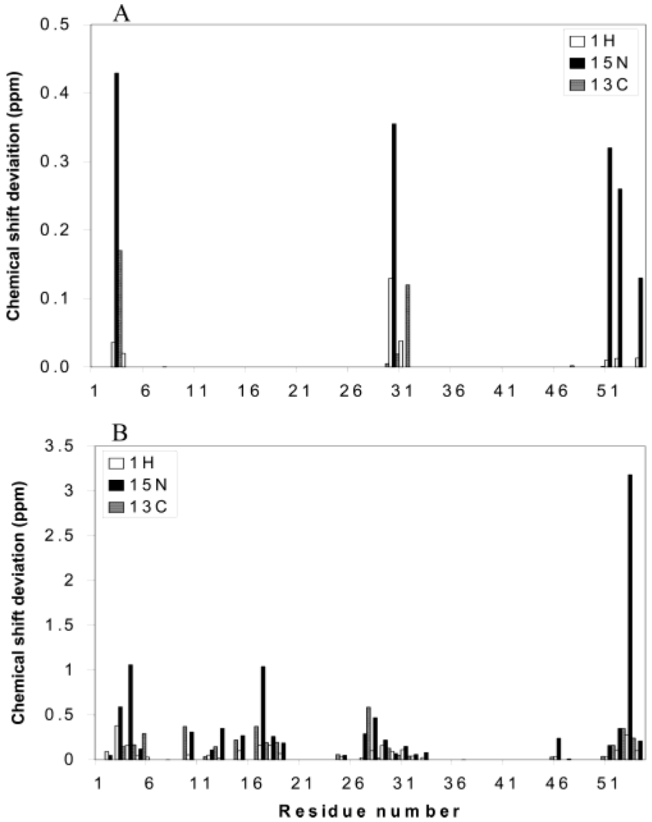

FIGURE 2: Effect of mutation of residue 1 on chemical shifts: (A) Met and fMet forms of CpRd; (B) Met, fMet, and wt forms of PfRd. ^{1}H, ^{13}C, and ^{15}N chemical shift maximum deviations are reported.

tion between the E15 carboxylic side chain and the A2 amide proton(s), as well as the salt bridge between K46 and E31 side chains, could be responsible for the propagation of the single N-terminal modification. Nevertheless, analysis of chemical shift temperature gradients between 10 and 70 °C showed no significant differences between the different CpRd/PfRd forms and the major fMet species (data not shown). These results, in agreement with thermostability studies on PfRdFe (*32*), suggest that the presence of methionine or formylmethionine in position 1, and thus the interactions affected by its modification, or deletion, is not a determinant to rubredoxin stability. Consequently, the study will focus on the major N-terminal formylmethionine forms of CpRdZn and PfRdZn.

Hydrogen Bond Network in Rubredoxins through $^{h3}J_{NC'}$ *Scalar Couplings.* Figure 1 shows the downfield regions of 2D S^3 HNCO-TROSY spectra collected at 25 °C under the same conditions for both proteins. In addition to cross-H-bond and residual one-bond correlations, a significant number of correlations corresponding to intraresidue $^2J_{NC'}$ and, in the case of Asn or Asp residues, $^3J_{NC'}$ scalar couplings are detected. Focusing on the cross-H-bond correlations, seven are clearly identified in the case of CpRdZn while five only are observed in PfRdZn. All of them arise from hydrogen bonds between backbone amide protons and backbone carbonyl carbons; no backbone to side-chain correlation could be detected with any of the sequences used in this study [including the CPD sensitivity-enhanced sequence by Liu et al. (*41*)].

After separate measurements of $^1J_{NC'}$ scalar couplings, quantification of the $^{h3}J_{NC'}$ values was pursued according to eq 1 mentioned in the Experimental Procedures. Values calculated from different experimental data sets are reported in Table 1 [$^2J_{NC'}$ and $^3J_{NC'}$ scalar couplings determined in a similar manner are reported in Supporting Information (Table S5)]. Error estimates based on signal-to-noise level and standard propagation analysis were lower than error estimates based on experiment reproducibility. Accuracy of $^{h3}J_{NC'}$ depends in particular on the value of the constant time delay allowed for de/rephasing ^{13}C magnetization but also on the value of additional couplings such as $^2J_{NC'}$ and $^3J_{NC'}$. As a consequence, errors reported in Table 1 were based on divergence of values determined from at least two or three different data sets.

To date, seven (respectively five) solid-state structures and one (respectively one) NMR solution structure have been deposited in the RCSB database for different forms (Zn, Fe^{III}, Fe^{II}) of Cp (respectively Pf) rubredoxin (mutations excluded). The resolution of crystal structures varies from 0.95 to 1.8 Å (PDB codes 1irn, 1iro, 5xrn, 4xrn, 1fhh, and 1fhm for CpRd and 1bq8, 1bq9, 1brf, 1caa, and 1cad for PfRd). All of them were individually examined with the Chimera package from the Computer Graphics Laboratory, University of California, San Francisco (supported by NIH Grant P41 RR-01081) (*83*) to identify hydrogen-bonding patterns, using a cutoff of 3.35 Å for the $R_{N\cdots O}$ distance (corresponding to the relaxation of distance and angular constraints by 0.4 Å and 20° within Chimera). Despite a sensible variation of geometric characteristics, the presence of 24 (respectively 27) hydrogen bonds arising from backbone amide protons was consistently established for CpRd (respectively PfRd) in all studied structures. $R_{H\cdots O}$ and $R_{N\cdots O}$ distances and θ_{NHO} and θ_{HOC} angles as well as ρ_{HOCN} dihedral angles are reported in Table 1 (and Table S8 in Supporting Information) for the structures of highest resolution (PDB codes 1irn, resolution 1.2 Å for Met-CpRdZn, and 1bq9, resolution 1.2 Å for fMet-PfRdFe). Maximum deviations in these values over the ensemble of structures are also included. The number of proposed hydrogen-bonding interactions in the solid state contrasts sharply with the small number of hydrogen bonds detected in our study in solution. As such, it differs from previous reports on proteins of comparable size like ubiquitin (*36*, *51*), protein G (*42*, *52*), and cold shock protein A (*45*). Previous measurement of backbone N−H residual dipolar couplings in a suspension of filamentous bacteriophage Pf1 (*28*) at 25 and 70 °C indicates that the basic structure in solution is in good agreement with the structures observed in the crystalline state, ruling out major differences of conformations between the two states. Instead, the absence of extended, highly regular secondary structure elements in rubredoxins is considered a major cause of the differences. In fact, in ubiquitin, protein G, and cold shock protein A, more than 50% of the residues are involved in either β-sheets or α-helices, with typical θ_{NHO} and θ_{HOC} angle values of 150−180° and 140−180°, respectively. In rubredoxin, by comparison, only 15% of the residues are engaged in a regular secondary structure element. As a result the NHO angle and more importantly the HOC angle depart markedly from linear geometry, as shown in Table 1 (and Table S8). According to quantum chemical calculations (*46*, *49*, *50*), the quadratic dependence of the interresidue coupling on cos θ_{HOC} causes a drastic decrease of $^{h3}J_{NC'}$ values, and calculations on the formamide dimer imply that $^{h3}J_{NC'}$ would vanish near $\theta_{HOC} = 130/235°$ for a typical $R_{H\cdots O}$ distance of 2.0 Å. When this angular restriction is taken into account, together with the exponential decrease in $^{h3}J_{NC'}$ as a function of $R_{N\cdots O}$ distance (*42*), the number of potentially detectable hydrogen bonds drops to 9 in the case of CpRd and 12 in the case of PfRd (Table 1). Differences between these expectations and the actual number of detected hydrogen bonds are believed to arise from subtle but real conformational changes in solution.

An example of a possible difference in solution can be seen in the hydrogen bond between the nitrogen donor of residue G27 and the oxygen acceptor of residue 15. This hydrogen bond is expected, according to crystal structures, to present the shortest $R_{N\cdots O}$ distance (2.67 and 2.66 Å, respectively, in CpRd and PfRd) and thus, according to Cornilescu et al. (*42*), the largest $|^{h3}J_{NC'}|$ value (1.29 ± 0.43 and 1.09 ± 0.30 Hz, respectively, in CpRd and PfRd) (see Table 1). Inclusion of the angular dependence (eq 14 in ref *50*) on the basis of the X-ray structure does not improve the correlation to the observed $|^{h3}J_{NC'}|$ value of ∼0.4 Hz in CpRd and the absence of any through-hydrogen bond coupling in the case of PfRd within the signal-to-noise limit (a $|^{h3}J_{NC'}|$ value lower than 0.2 Hz). Instead, elongation of the $R_{N\cdots O}$ distance to 2.75 Å and a slight decrease of θ_{HOC} to 162° would give rise to the observed scalar coupling of 0.45 Hz.

The sensitivity of $^{h3}J_{NC'}$ coupling to detailed hydrogen bond geometry in solution makes it an ideal parameter to evaluate and compare the extent and strength of the hydrogen bond network in CpRd and PfRd. Strong hydrogen bonds, depicted in Figure 3, are detected mainly in the triple-stranded β-sheet (residues 5, 6, 7, 13, 50, and 52 in Table 1) as well as at the

Table 1: X-ray and NMR (25 °C) Parameters Related to Hydrogen Bonds Involving the Backbone Amide in Cp and Pf Rubredoxins[a]

	donor						acceptor				hydrogen bond						
^1H_N	$^1J_{NH}$[b] (Hz) (error)	$^1J_{NC'}$[b] (Hz) (error)	^1H CSD[c] (ppm)	^{15}N CSD[c] (ppm)	^1H $\Delta\delta/\Delta T$[d] (ppb/K)	^{15}N $\Delta\delta/\Delta T$[d] (ppb/K)	^{13}C	$^1J_{NC'}$[b] (Hz) (error)	^{13}C CSD[c] (ppm)	^{13}C $\Delta\delta/\Delta T$[d] (ppb/K)	$R_{H\cdots O}$[e] (Å)	$R_{N\cdots O}$[e] (Å)	θ_{NHO}[e] (deg)	θ_{HOC}[e] (deg)	ρ_{HOCN}[e] (deg)	$^{h3}J_{NC'}$ (Hz) calc[f]	$^{h3}J_{NC'}$ (Hz) obs[g]
CpRd																	
T5	93.27	14.35	1.24	1.97	−1.76	−1.91	E50	14.65	−1.28	3.14	2.066	2.906	165.2	154.3	−150.8	−0.53	−0.79
	(0.38)	(0.43)						(0.52)			(0.285)	(0.142)	(5.0)	(2.3)	(33.6)	−0.71	(0.02)
C6	94.34	14.95	1.09	12.70	−3.05	5.51	Y11	16.02	−2.16	3.55	2.004	2.851	168.1	160.5	154.2	−0.66	−0.79
	(0.29)	(0.26)						(0.30)			(0.283)	(0.227)	(3.2)	(3.8)	(7.8)	−0.88	(0.08)
T7	94.59	14.28	0.09	3.65	−3.82	−12.81	Q48	15.41	−0.44	0.67	2.165	2.986	159.4	144.2	−66.1	−0.38	
	(0.36)	(0.26)						(0.30)			(0.241)	(0.191)	(4.8)	(6.2)	(15.5)	−0.56	
Y13	91.95	13.49	1.34	2.33	−3.64	3.41	Y4	14.41	−1.87	3.65	1.988	2.777	152.1	166.2	106.8	−0.88	−0.94
	(0.07)	(0.26)						(0.31)			(0.183)	(0.107)	(5.4)	(4.6)	(41.5)	−1.11	(0.09)
G18	94.89	15.23	−0.29	−1.30	−3.21	−13.78	N14	13.83	1.42		2.229	2.954	142.0	150.5	−6.8	−0.44	
	(0.14)	(0.39)						(0.21)			(0.150)	(0.082)	(10.2)	(6.0)	(25.1)	−0.59	
G27	94.24	16.17	0.12	5.50	−0.89	−12.16	P15		0.18	−0.49	1.867	2.674	155.6	164.1	−39.1	−1.34	−0.44
	(0.08)	(0.43)									(0.173)	(0.104)	(9.5)	(2.2)	(43.4)	−1.14	(0.10)
C39	93.96	14.81	1.25	−0.08	−2.89	0.90	V44	16.29	−2.30	0.13	2.026	2.873	168.4	157.4	−173.1	−0.60	−0.91
	(0.27)	(0.29)						(0.34)			(0.282)	(0.139)	(1.7)	(4.7)	(18.3)	−0.82	(0.05)
E50	93.18	14.65	0.68	−2.57	−1.59	1.15	T5	14.35	−3.12	−3.39	2.179	2.988	156.5	147.1	−146.6	−0.38	−0.47
	(0.04)	(0.52)						(0.43)			(0.222)	(0.163)	(4.7)	(5.9)	(5.8)	−0.49	(0.02)
V52	93.42	15.32	0.36	6.44	−3.82	−32.8	K3	14.86	−0.37	−5.02	2.014	2.865	170.7	147.4	57.7	−0.62	−0.38
	(0.46)	(0.17)						(0.21)			(0.209)	(0.105)	(7.3)	(6.0)	(16.1)	−0.81	(0.07)
PfRd																	
V5	92.88	14.65	1.37	1.85	−2.32	−7.63	E50	14.53	−1.95	6.60	1.972	2.850	171.8	159.9	−139.7	−0.66	
	(0.17)	(0.17)						(0.09)			(0.068)	(0.083)	(9.8)	(5.5)	(8.2)	−0.82	
C6	94.53	14.35	1.26	9.88	−3.05	4.34	Y11	16.20	−3.18	4.74	1.937	2.846	176.5	166.9	−178.8	−0.67	−1.10
	(0.63)	(0.17)						(0.39)			(0.039)	(0.041)	(6.5)	(7.5)	(13.9)	−0.93	(0.04)
K7	95.46	14.28	0.82	7.72	−6.91	−14.87	E48	15.74	−2.16	4.88	1.934	2.823	165.2	158.3	−57.6	−0.74	−0.67
	(0.06)	(0.09)						(0.17)			(0.069)	(0.069)	(4.7)	(10.1)	(21.1)	−0.49	(0.02)
Y13	92.40	13.22	1.34	3.25	−3.94	3.18	W4	14.92	−2.25	3.98	1.987	2.739	139.0	156.4	113.8	−1.03	−1.16
	(0.01)	(0.47)						(0.39)			(0.066)	(0.046)	(6.7)	(9.9)	(40.3)	−1.12	(0.05)
E15	93.52	14.74	0.26	5.07	−2.50	−6.48	A2	15.74	−1.76	−0.94	2.050	2.933	163.4	168.6	−17.5	−0.47	
	(0.56)	(0.30)						(0.43)			(0.073)	(0.084)	(7.6)	(5.4)	(66.1)	−0.34	
G18	94.85	14.68	0.09	−1.34	−2.91	−11.31	D14	14.16	1.22	−2.04	2.241	2.964	136.1	152.7	5.7	−0.42	
	(0.44)	(0.39)						(0.17)			(0.181)	(0.107)	(15.1)	(4.3)	(2.8)	−0.46	
G27	94.56	16.02	−0.35	6.80	−4.15	−17.36	E15	14.74	1.80	−1.22	1.916	2.659	137.4	162.3	28.5	−1.42	
	(0.15)	(0.30)						(0.30)			(0.160)	(0.118)	(11.7)	(5.8)	(45.5)	−2.09	
C39	93.96	14.92	1.25	0.33	−2.09	5.49	A44	16.17	−1.17		1.920	2.822	170.4	146.8	−152.5	−0.74	−0.81
	(0.15)	(0.21)						(0.34)			(0.066)	(0.043)	(8.5)	(14.4)	(13.3)	−0.62	(0.01)
E50	93.62	14.53	0.44	−1.79	−1.32	−14.04	V5	14.65	−3.03	1.46	2.101	2.969	158.9	147.3	−153.8	−0.41	
	(0.20)	(0.09)						(0.17)			(0.080)	(0.132)	(11.5)	(6.0)	(15.7)	−0.59	
L52	94.17	14.89	0.76	6.49	−4.85	−14.9	K3	15.53	−1.78	1.24	1.925	2.818	166.6	151.8	24.8	−0.75	−0.52
	(0.06)	(0.09)						(0.04)			(0.036)	(0.048)	(8.6)	(12.3)	(29.7)	−0.91	(0.06)

[a] Hydrogen bond description in the present table is limited to hydrogen bonds supported by or relevant to our study. A full table is given in Supporting Information (Table S8). [b] Average values and errors obtained from a ^{15}N-coupled [^{1}H,^{15}N]-HSQC and a [^{1}H,^{15}N]-IPAP-HSQC collected with gradient sensitivity enhancement for $^1J_{NH}$ and from two independent ^{13}C-coupled [^{1}H,^{15}N]-HSQC for $^1J_{NC'}$. [c] CSD $= \delta_{obs} - \delta_{rc} - \delta_{ring}$ for ^{1}H and CSD $= \delta_{obs} - \delta_{rc}$ for ^{13}C and ^{15}N, where δ_{ring} is calculated using Shifts 4.1 from Case et al. using PDB code 1irn for CpRd and PDB code 1bq9 for PfRd and where $\delta_{rc} = \delta_{rc-crude} + D_{i-2} + C_{i-1} + B_{i+1} + A_{i+2}$ with A, B, C, D, and $\delta_{rc-crude}$ taken from Shwarzinger et al. (*71*, *72*) to correct for sequence effects. Estimated errors on observed chemical shifts are 0.015 ppm for ^{1}H and 0.2 ppm on ^{13}C and ^{15}N. [d] Slope of the chemical shift dependence as a function of temperature after linear regression analysis. [e] Distances and angles are extracted from the PDB files 1irn (resolution 1.2 Å, pH = 4.0, Met-CpRdZn) for CpRd and 1bq9 (resolution 1.2 Å, pH = 8.5, fMet-PfRdFe) for PfRd. Errors indicated within parentheses represent the maximum deviations observed in the other structures examined. In the case of CpRd RMSD values for backbone heavy atoms were 0.226, 0.308, 0.313, 0.285, and 0.480 Å between 1irn and 1iro, 1irn and 4xrn, 1irn and 5xrn, 1irn and 1fhh, and 1irn and 1fhm, respectively. In the case of PfRd RMSD values for backbone heavy atoms were 0.253, 0.112, 0.129, and 0.370 Å between 1bq9 and 1bq8, 1bq9 and 1brf, 1bq9 and 1caa, and 1bq9 and 1cad, respectively. [f] The first scalar coupling value for each residue is calculated on the basis of the empirical formula proposed by Cornilescu et al. (*42*): $^{h3}J_{NC'} = -59000 \exp(-4R_{N\cdots O})$. The second value refers to the more complete description proposed by Barfield (*50*): $^{h3}J_{NC'} = [-0.84 \cos^2 \theta_{HOC} + (-0.66 \cos^2 \rho_{HOCN} + 0.17 \cos \rho_{HOCN} - 0.35) \sin^2 \theta_{HOC}] \exp[-3.2(R_{N\cdots O} - 2.88)] + 0.06$. [g] Scalar couplings are measured using the S^3 HNCO-TROSY pulse sequence proposed by Meissner and Sørensen (*39*). Errors are given within parentheses.

metal site (residues 6 and 39 in Table 1). In these two regions Cp and Pf rubredoxins show subtle but definite differences: first, in the number and nature of hydrogen bonds between the three strands of the β-sheet and, second, in the strength of these interactions. In fact, the topology of the hydrogen-bonding network between the N-terminal (strand 1) and the C-terminal (strand 3) fragments changes from three consecutive bonds in CpRd (K3→V52, T5→E50, E50→T5) to two discretely located bonds in PfRd (K3→L52, K7→E48). In addition, the hydrogen bond T5→E50 appears unexpectedly strong in CpRd. This is not compensated in PfRd by the newly formed K7→E48 bond, implying an overall weaker interaction between strands 1 and 3 in PfRd. In contrast, strands 1 and 2 interact in both proteins through two homologous hydrogen bonds involving the amide hydrogens of C6 and Y13 with the carbonyls of residues Y11 and Y/W4, respectively. $^{h3}J_{NC'}$ scalar couplings in PfRd, however, increase by ~10% compared to their value in CpRd, suggesting a stabilization of the interactions in the hyperthermostable protein. At the metal site, the change of V44

```
          5        10        15       20        25       30       35        40       45       50
Cp   MKKYT CTVCG YIYNP EDGDP DNGVN PGTDF KDIPD DWVCP LCGVG KDQFE EVEE
Pf   MAKWVCKICG YIYDE DAGDPDNGIS  PGTKF EELPD DWVCP ICGAP KSEFE KLED
```

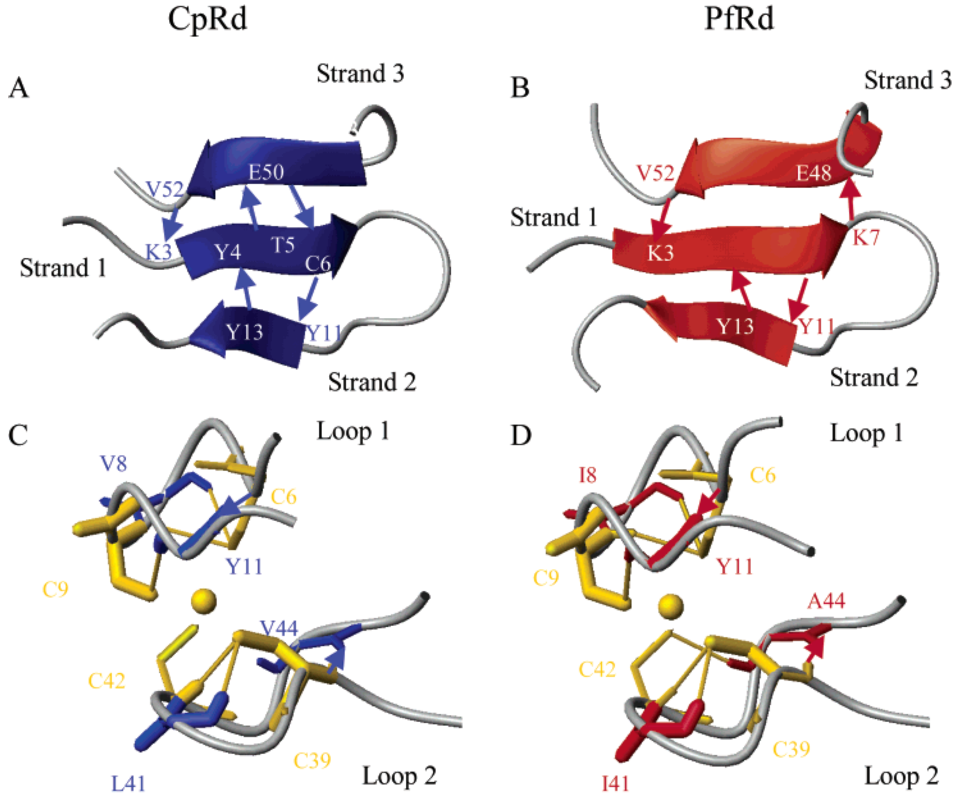

FIGURE 3: Comparison of Cp and Pf rubredoxin hydrogen-bonding patterns in solution: (A, B) in the three-stranded β-sheet; (C, D) at the metal binding site. The fMet form of each protein only is considered. Data for CpRd are coded in blue (A, C) and data for PfRd are coded in red (B, D). N−H···O=C hydrogen bonds are sketched with arrows going from the amide donor to the carbonyl acceptor. NH···S(Cys) hydrogen bonds are represented in cyan. Gold denotes for cysteine ligands and the metal. This figure was prepared within the program MOLMOL (*95*), using available crystal structures from the RCSB databank (PDB code 1irn for CpRd and PDB code 1bq9 for PfRd). In part B, amino acid designation is from CpRd. The following change occurs for PfRd: The label V52 should be replaced by L52.

in CpRd into an alanine residue in PfRd tends to weaken the hydrogen bond between the residue 44 carbonyl group and the amide proton of residue C39. This contrasts with the apparent strengthening of the C6→Y11 hydrogen bond in PfRd. Interestingly, the V44A mutation has been correlated with changes in redox potential between the two rubredoxins (*25*, *26*).

One additional through-hydrogen bond correlation is detected only in CpRd. That correlation involves residues located in the coil of CpRd between residues 27 and 15. Positioned at the other end of the tertiary structure compared to the metal site, this bond locks the end of strand 3 to the upstream part of the second 3_{10}-helix in CpRd. In contrast to the crystal structure, the equivalent interaction in PfRd is weaker and remains beyond detection. In the same region, an additional hydrogen bond has been suggested to be exclusively present in PfRd. That bond is between the amide of F30 and the carboxylic side chain of E15. This bond has been proposed to play a crucial role in the protein thermostability (*20*, *30*, *84*). Despite the expectation of a larger Fermi contact contribution to the scalar coupling due to the presence of a negative charge on the acceptor oxygen atom (*85*), no connection could be detected in our experiments.

Hydrogen Bonds and Other NMR Parameters. A number of other NMR parameters have been considered as potential indicators of hydrogen bonds in proteins, including isotropic (*86*) and anisotropic (*87*, *88*) amide ^{1}H chemical shifts as well as the sequential one-bond $^{1}J_{NC'}$ scalar couplings (*89*). More recently, correlations have been proposed between $^{h3}J_{NC'}$ and ^{1}H chemical shifts as both depend on the hydrogen bond length (*51*, *45*, *50*) and between $^{h3}J_{NC'}$ and $^{1}J_{NC'}$ as the latter is increased (respectively decreased) when the carbonyl (respectively amide) group experiences interaction as an acceptor of a hydrogen atom (*89*, *90*).

Amide ^{1}H chemical shift deviations [CSD $= \delta_{obs} - \delta_{rc} - \delta_{ring}$, where the random coil value δ_{rc} is corrected for sequence effects and the calculated ring current shifts (δ_{ring}); see Experimental Procedures] have been calculated to try to separate the hydrogen bond contribution from factors such as the nature of the amino acid and the ring current shift effects arising from the structural proximity of aromatic side chains. Corresponding values are reported in Table 1. Residues 5, 6, 13, and 39 show in both proteins positive CSD values greater than 1 ppm, in agreement with the relatively strong $^{h3}J_{NC'}$ values detected in the long-range HNCO experiments described previously. Furthermore, shifts toward higher (respectively lower) CSD values are observed for residues 7 and 52 (respectively 27 and 50) when going from CpRd to PfRd, which is consistent with the substantial strengthening (respectively weakening) of hydrogen bonds

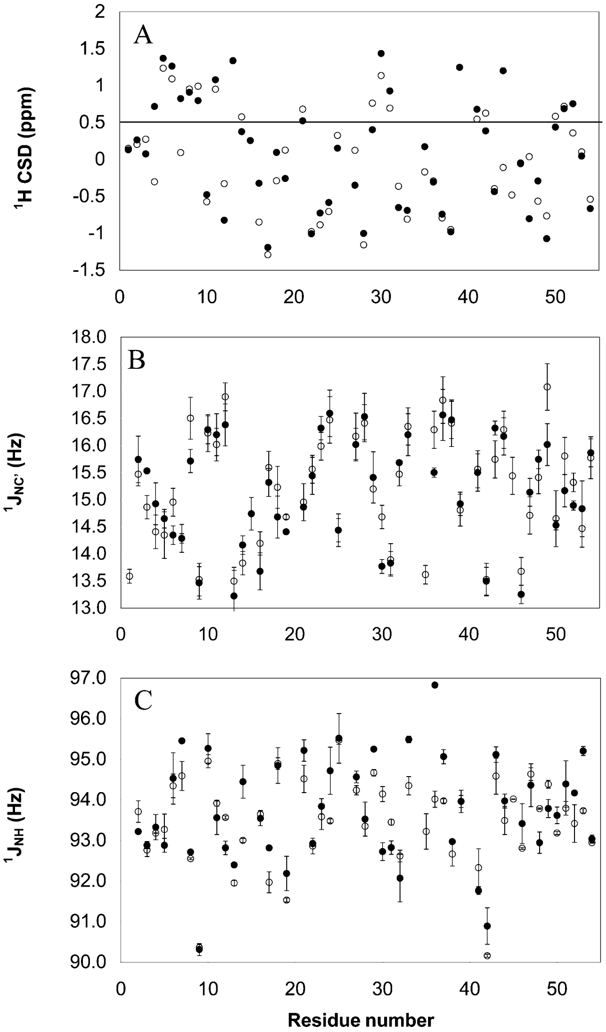

FIGURE 4: Comparison of different NMR parameters in CpRd (open circles) and PfRd (filled circles) rubredoxins: (A) ^{1}H chemical shift deviations (CSD, CSD = $\delta_{obs} - \delta_{rc} - \delta_{ring}$, where δ_{rc} is the random coil value corrected for sequence effects and δ_{ring} is the ring current effect calculated within Shifts 4.1); (B) $^1J_{NC'}$ scalar couplings; (C) $^1J_{NH}$ scalar couplings. The fMet form of each protein only is considered.

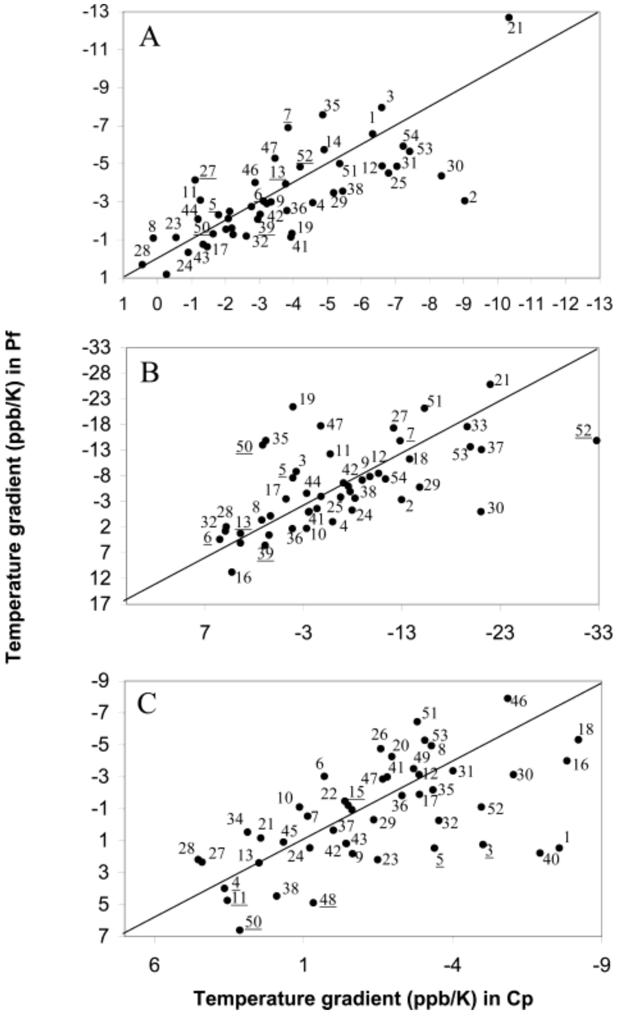

FIGURE 5: Comparison of chemical shift temperature gradients ($\Delta\delta/\Delta T$ in ppb/K) in Cp and Pf rubredoxins: (A) ^{1}H; (B) ^{15}N; (C) ^{13}C. The fMet form of each protein only is considered.

noticed in the $^{h3}J_{NC'}$ analysis. These results translate into a reasonable linear correlation ($r^2 = 0.90$) between the $^{h3}J_{NC'}$ and the CSD values, in cases where through-hydrogen bond correlations are unambiguously detected. Despite the absence of through-hydrogen bond couplings, additional residues show relatively large CSD values (close to or larger than 1 ppm), namely, residues 8, 9, 11, 30, and 31 in both rubredoxins as well as alanine 44 in PfRd (see Figure 4A). Interestingly, residues 8, 9, 11, 41, 42, and 44 have been proposed to be involved in NH···S(Cys) hydrogen bonding, and five of these residues (8, 9, 11, 41, 42) have been shown to exhibit a two-bond hydrogen-to-metal scalar coupling in a ^{113}Cd-substituted Pf rubredoxin (*21*). The drastic change in the CSD value for alanine 44, as well as its rather large value of 1.20 ppm, thus suggests the existence of six NH···S(Cys) hydrogen bonds in Zn-substituted Pf rubredoxin against five only in Cp rubredoxin. This result is in agreement with the short N···S(Cys) distance (3.53 Å) observed in the 1.2 Å resolution crystal structure of fMet-PfFeRd (PDB code 1bq9) in comparison to the equivalent distance (3.76 Å) in MetCpRdZn (PDB code 1irn). The fairly large CSD value observed for F30, on the other hand, is more difficult to rationalize. The contribution of the proposed hydrogen bond between the F30 amide and the E15 glutamate side chain could be proposed, as correlation plots between F30 amide proton and nitrogen shifts show a smaller chemical shift temperature gradient in PfRd versus CpRd (see Figure 5A,B) (*91*). Nevertheless, the origin of the high CSD value in CpRd and the relatively small difference between CpRd and PfRd remain unclear.

Hydrogen bonding is also expected to produce deshielding effects on carbonyl ^{13}C and amide ^{15}N resonances (*92*); these nuclei are nevertheless very sensitive to local structure (ϕ and ψ angles), and separation of the different contributions from hydrogen bonds would require extensive new ab initio calculations because of the absence of regular secondary structure elements in the rubredoxins (data not shown).

One-bond $^1J_{NC'}$ scalar couplings are modulated by molecular conformation (ϕ and ψ angles) and hydrogen-bonding effects either to the carbonyl (increase of $|^1J_{NC'}|$) or to the amide (decrease of $|^1J_{NC'}|$) (*47*, *89*). Quantum calculations on ubiquitin fragments (*49*) suggest that the subtle balance between monomer relaxation effects and electronic cloud deformation also contributes to the variations of $^1J_{NH}$ scalar coupling with hydrogen-bonding geometry. As such, extreme caution should be taken with respect to their interpretation in an absolute manner (*47*). Nevertheless, if conformations of two proteins are very similar, as in the case of Cp and Pf rubredoxins, they may be adequate indicators of the increase or decrease of hydrogen bond interaction strengths. In this context, $^1J_{NC'}$ coupling constants for both proteins are plotted on the same scale in Figure 4B. For most residues, values in CpRd and PfRd are identical within 0.5 Hz. Among the few exceptions, F30 shows a smaller $|^1J_{NC'}|$ constant, which could be another indication of the proposed interaction between the F30 amide and the E15 carboxyl side chain mentioned in the proton chemical shift analysis. In a similar sense, increased interaction between the V8 carbonyl group and a water molecule could tentatively explain the significantly increased $|^1J_{NC'}|$ value measured in CpRd. This observation is in agreement with greater solvent accessibility proposed at this residue by Bonomi et al. (*93*). With respect to the hydrogen-bonding network discussed above, comparison of $^1J_{NC'}$ values suggests enhanced donating (lower $|^1J_{NC'}|$) and reduced accepting (lower $|^1J_{NC'}|$ for residue $i + 1$) capacities, respectively, for residues C6 and L52 and residues V5, E15, E48, and E50 in PfRd (Figure 4B). The resultant strengthening of C6→Y11 and L52→K3 hydrogen bonds, as well as weakening of V5→E50, G27→E15, and E50→V5 hydrogen bonds, is in agreement with the $^{h3}J_{NC'}$ study mentioned earlier. The increased accepting capacity of Q48 in CpRd, however, cannot be explained by a strengthening of the T7→E48 bond, as the corresponding correlation is absent in the long-range HNCO experiment. The high $|^1J_{NC'}|$ value (above 17 Hz) observed for residue F49 in CpRd instead suggests hydrogen bonding to a hydroxyl group (*89*). According to the high-resolution crystal structure (PDB code 1irn), the T7 hydroxyl group is a good candidate as it is located at 2.745 Å from the E48 carbonyl group ($R_{O\cdots O}$ distance). To conclude, differences between CpRd and PfRd emphasized by the present $^1J_{NC'}$ data are in complete agreement with respect to the interactions obtained from the $^{h3}J_{NC'}$ study, i.e., changes in the nature and strength of hydrogen-bonding network between strand 1 and strand 3 in the triple-stranded β-sheet (Figure 3).

In both rubredoxins, cysteines 9 and 42 exhibit small $|^1J_{NC'}|$ (13.55 ± 0.05 Hz, Figure 4B) as well as $|^1J_{NH}|$ (90.43 ± 0.32 Hz, Figure 4C) values. As no comparable effect is observed for the other candidates for NH···S(Cys) hydrogen bonds mentioned in the chemical shift analysis, a polarization effect arising from the metal is believed to cause the decrease in the one-bond scalar couplings. As it turns out from the crystal structures, the C9 and C42 amide nitrogens are located in close proximity (3.8 ± 0.2 Å) to the metal center. If this assessment is correct, these couplings could potentially monitor distortions at the metal center. In the present study, the -90.89 Hz $^1J_{NH}$ coupling constant measured for C42 in PfRd (instead of -90.16 Hz in CpRd) might indicate a small conformational change, which moves this residue slightly away from the metal site. Nevertheless, as the average deviation between CpRd and PfRd is 0.54 Hz, verification of this suggestion may require a quantum mechanical modeling study including vibrational contributions to the N−H bond.

Temperature Dependence and the Hydrogen Bond Network. The changes in NMR parameters, namely, chemical shifts and through-hydrogen bond scalar couplings, as a function of temperature are considered in this section. ^{1}H, ^{15}N, and ^{13}C chemical shifts have been extracted from 2D [^{1}H,^{15}N]-HSQC and HNCO acquired over the range 10−70 °C for CpRd and 10−80 °C for PfRd. Despite small departures from linearity observed in a small number of residues for carbonyl carbons and amide nitrogens (residues 6, 32, 44, 45 and 5, 35, 43, 50, respectively, in CpRd; residues 6, 10, 27, 43, 53 and 2, 10, 13, 24, 32, 43, 50 respectively, in PfRd), most amide nitrogens and carbonyl carbons as well as all backbone amide protons showed a linear temperature dependence of chemical shift.

When slopes are compared in CpRd and PfRd, backbone ^{1}H, ^{15}N, and ^{13}C chemical shift temperature gradients ($\Delta\delta/\Delta T$) show a striking similarity (Figure 5). Residues located in the N-terminal (residues 1−5, 7) and C-terminal (residues 48, 50, 52) end of the protein and a limited number of discrete residues (19, 27, 30, 35, 40, 47) nevertheless exhibit significant differences. Opposite temperature gradients are in particular observed in CpRd vs PfRd for K3 and T/V5 carbon nuclei as well as for the E50 nitrogen. Added to the increased temperature gradient observed for V52 and the E50 nitrogen, respectively, in CpRd and PfRd, this provides good evidence for an alteration of the interaction between strand 1 (N-terminal) and strand 3 (C-terminal) of the three-stranded β-sheet in Cp versus Pf rubredoxin. In the same vein, the larger temperature gradient observed for the G27 amide proton in PfRd could be tentatively associated with the absence of the G27→E15 hydrogen bond suggested on the basis of the scalar coupling studies. The lower F30 amide proton and nitrogen gradients in PfRd could also arise from the presence of a hydrogen bond from the F30 amide to the side chain of the same residue, as proposed on the basis of X-ray data and found consistent with our ^{1}H CSD analysis. Furthermore, strong carbonyl acceptors and nitrogen donors involved in hydrogen bonds tend to show positive temperature gradients, while protons exhibit small negative gradients (absolute value less than 4 ppb/K). Nevertheless, interpretation of the sign and amplitude of chemical shift temperature gradients in terms of hydrogen bonds (*91*) remains hazardous in proteins that lack secondary structure elements. As an example, there is no evidence, based on the temperature gradient data, that the hydrogen bond K7→E48 is much stronger and the hydrogen bond V5→E50 is much weaker in PfRd. In addition, no quantitative correlation could be drawn between the chemical shift temperature gradients and the measured $^{h3}J_{NC'}$ scalar couplings. Extraction of the different contributions to chemical shift would be required for an extensive and detailed analysis of the temperature gradients.

Long-range HNCO experiments have been collected with the same parameter sets at 10, 25, and 40 °C for CpRd and PfRd (an additional temperature of 50 °C has been collected for PfRd). Every long-range HNCO experiment yielded the same set of through-hydrogen bond connectivities, with only one exception: the V52→K3 cross-correlation remained undetected at 10 °C in the CpRd sample (data not shown). Further quantification of cross-correlations suggested mainly invariant $^{h3}J_{NC'}$ coupling constants in the range 10−40 °C (Supporting Information, Table S6). In CpRd, only the hydrogen bond C39→V44 at the metal binding site and V52→K3 between strands 1 and 3 of the β-sheet presented a tendency toward a decrease and an increase of the $^{h3}J_{NC'}$ absolute value, respectively (0.14 Hz on the temperature range studied). The observed trends in PfRd are either of weaker amplitude (for C39) or of opposite sign (for L52). This suggests that the interaction between the N-terminal end of strand 1 and the C-terminal end of strand 3 is reinforced in CpRd while weakened in PfRd as the temperature is increased (Figure 3). The other difference with respect to temperature response of the proteins is found at the metal site. In both proteins residues C6 and C39 are related through a pseudo-C_2 symmetry axis located at the zinc atom and so are the hydrogen bonds C6→Y11 and C39→V/A44 (Figure 3). In CpRd, the hydrogen bond C39→V44 is stronger (larger ${}^{h3}J_{NC'}$ absolute value) than its symmetric partner C6→Y11 at low temperature, and as the temperature is increased, the strength of these two bonds tends to converge. On the contrary in PfRd, the hydrogen bond C39→A44 is weaker (lower ${}^{h3}J_{NC'}$ absolute value) than its symmetric partner C6→Y11 at low temperature and remains so up to at least 50 °C (Table 1 and Supporting Information, Table S6). The impact of such change in the hydrogen bond network at the metal site is discussed below.

DISCUSSION

In the solid state, the backbone atoms of the structures of CpRd (Met form, PDB code 1irn) and PfRd (fMet form, PDB code 1bq9) rubredoxins have a RMSD of 0.648 Å. This translates into the conservation of the hydrogen bond network from one species to the other with only one exception. The framework carrying the E15 side-chain carboxylate, W4 ring imino group, and A2/F30 amide groups in PfRd is replaced by two discrete backbone hydrogen bonds, T28→N25 and K31→D29$_\gamma$, in CpRd. The structural similarity between the two structures is also preserved in solution below the CpRd denaturation transition (*28*). Nevertheless, detailed analysis of NMR parameters such as chemical shifts and scalar couplings, ${}^{1}J_{NH}$, ${}^{1}J_{NC'}$, and especially ${}^{h3}J_{NC'}$, clearly points to definite differences that extend beyond the E15 framework. These include differences in the three-stranded β-sheet, in the metal site, and in the multiple-turn region comprised of residues 27−32 (Figure 3).

Considering the three-stranded β-sheet first, strong hydrogen bonds, C6→Y11 and Y13→Y4 (${}^{h3}J_{NC'}$ scalar couplings larger than 0.8 Hz), characterize the interaction between strands 1 and 2 in both proteins. They also seem to remain intact up to 70 °C in both rubredoxins, according to the ${}^{h3}J_{NC'}$ scalar coupling measurements and the chemical shift temperature dependence (Figure 5). When values in CpRd are compared to those in PfRd, however, the ${}^{h3}J_{NC'}$ scalar coupling constants in PfRd exhibit a 20% increase, which in terms of hydrogen bond length correspond to a 0.05−0.08 Å contraction (*42*). Assuming that the energetic contribution of a N−H···O═C hydrogen bond varies from 3.7 to 5.8 kcal·mol^{-1} over a 0.4 Å change in length (*49*), this leads to a 0.25−0.4 kcal·mol^{-1} energy stabilization in PfRd. Establishing a quantitative relationship between H-bond scalar couplings and energies of bonding is not straightforward. Nevertheless, it is believed that the dominant contribution to the through-hydrogen bond coupling constant ${}^{h3}J_{NC'}$ involves a direct electron-mediated mechanism between the N−H and O═C pairs and shows a quadratic dependence on the H···O overlap integral (*50*). As such, ${}^{h3}J_{NC'}$ scalar coupling is a direct measure of the hydrogen bond strength. Furthermore, a good correlation between this coupling constant and the binding energy has been evidenced in the case of the formamide dimer, suggesting that the former is to a large extent an indirect representation of the enthalpic contribution to hydrogen bonding (*49*).

The interaction between strands 1 and 3 in solution presents a quite different pattern within the two rubredoxins. In CpRd, there is a series of three hydrogen bonds extending from V52→K3 to E50→T5 to T5→E50. All of them are observed in the long-range HNCO experiment, and ${}^{h3}J_{NC'}$ scalar couplings can be measured. In PfRd, the observed hydrogen bonds begin at the same place (L52→K3) and extend further (K7→E48), but through-hydrogen correlations are not observed for the two intermediate pairs (E50→V5 and V5→E50). However, as in hydrogen bonds from the 1−2 strands, couplings are larger in PfRd for the conserved hydrogen bonds (−0.38 Hz in CpRd vs −0.52 Hz in PfRd for 52→3), and hence, this bond is presumably stronger. Furthermore, the extra K7→E48 bond in PfRd has a larger coupling (−0.67 Hz) than the average intermediate bonds in CpRd (−0.63 Hz). One might have considered the failure to observe couplings in the intermediate stretch an experimental problem; however, chemical shift data and ${}^{1}J_{NC'}$ scalar coupling data have been measured for these sites, and they support the idea that the hydrogen bonds are weaker. The net result of two to three stronger bonds and one missing hydrogen bond in PfRd is a small, if any at all, contribution to stability from this hydrogen-bonding network.

The metal binding site is defined by two β-turns (residues 6−11 and residues 39−44) related to each other through a pseudo-C_2 symmetry axis centered on the zinc atom. Each loop is characterized by a number of common features uniformly present in both proteins according to the present NMR data: one N−H$_i$···O═C$_{i+5}$ hydrogen bond ($i = 6$ in loop 1 and $i = 39$ in loop 2) identified in the long-range HNCO experiment and two or three NH$_i$···S(Cys)$_j$ hydrogen bonds ($i = 8$, $9/j = 6$ and $i = 11/j = 9$ in loop 1; $i = 41$, $42/j = 39$ in loop 2). These are proposed on the basis of the ^{1}H CSD of the corresponding amide protons. These hydrogen bonds seem to persist below the CpRd denaturation temperature, as suggested by the relatively small ^{1}H, ^{15}N, and ^{13}C temperature gradients as well as the detection of ${}^{h3}J_{NC'}$ scalar couplings at least up to 50 °C. However, a few differences become clearly evident on more detailed analysis. For one thing, a favorable interaction exists in PfRd between the A44 amide group and the C42 sulfur atom (as shown by the increase of ^{1}H CSD). This is correlated with the C42 amide group moving away from the metal as shown by the increase in ${}^{1}J_{NH}$ scalar couplings. The role of residue 44 as a modulator of the redox potential of the Fe(S-Cys)$_4$ site in native rubredoxins has already been supported by mutation of V44 in CpRd to A44 as found in PfRd (*26*). The present NMR study supports the idea that the strengthening of the hydrogen bond NH$_{44}$···S(Cys)$_{42}$, present in PfRd, is responsible for the movement of the coordinating sulfur and the 88 mV increase in redox potential. The other impact of the V44A substitution in comparing Cp to Pf is to cause a weakening of the 39→44 hydrogen bond as emphasized by the decrease of the corresponding ${}^{h3}J_{NC'}$ coupling in PfRd in comparison to CpRd. The strength of this interaction nevertheless remains constant in the temperature range of 10−50 °C, while the same bond weakens by 10−15% in

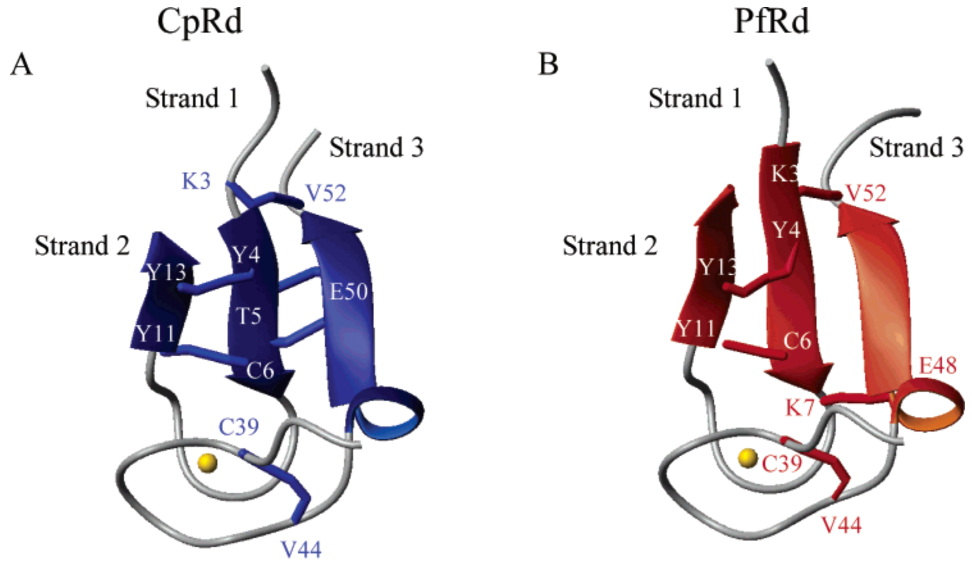

FIGURE 6: Repartition of HN···O=C hydrogen bonds between the metal binding site and the β-sheet in (A) CpRd and (B) PfRd. In part B, amino acid designation is from CpRd. The following changes occur for PfRd: The labels Y4, V52, and V44 should be replaced by W4, L52, and A44, respectively.

CpRd at 50 °C, making them nearly equivalent at 50 °C. Furthermore, when contributions of the NH$_{44}$···S(Cys)$_{42}$ hydrogen bond are added, an overall stabilization around the metal site is suggested in PfRd. Although no direct measurement allows quantification of the strength of the latter interaction, the resulting enthalpic contribution is believed to be more important than any contribution observed in the PfRd β-sheet.

Hydrogen bonds in the multiple-turn region of both rubredoxins (amino acids 14−32) appear to be extremely sparse, as indicated by the absence of long-range HNCO data. In fact, CpRd exhibits only one hydrogen bond, G27→P15. Although a hydrogen bond between the F30 amide and the side chain of residue E15 in PfRd is suggested by ^{1}H CSD and $^1J_{NC'}$ values, it remains undetected in the long-range HNCO experiment. As the $^{h3}J_{NC'}$ scalar coupling constants represent ensemble averages of the different conformational states and depend on individual hydrogen bond lengths, the present data agree with the existence of flexibility in both rubredoxins in the segment of residues 14−32 as proposed by Hernandez et al. (*84*).

Our investigation of hydrogen-bonding contributions to the enhanced thermal stability of PfRd was triggered by observations on chimera that substituted the first 15 residues in the native PfRd sequence with the residues from the Cp sequence (*15*, *28*). This piece included the 2-1-3 β-sheet segment and brought focus on hydrogen bonds in this segment. While there are variations in both the distribution and strength of hydrogen bonds in this segment, the detailed examination presented above does not support a strong contribution to net stabilization. However, this segment does carry metal center interactions (through residue 6) and does influence the size of the interaction through variations in the interactions between strands 1 and 3 (through residue 7). There are additional connections between the β-sheet and the multiple-turn region 14−32 (through residue 15). Thus, it appears likely that some stability contributions reside in the first 15 residues, but they cannot simply been ascribed to strengths of β-sheet hydrogen bonds. Instead, contributions seem to result from a redistribution of bonds culminating in metal center changes and optimal protection against metal loss for PfRd.

The indicators of enhanced stability for PfRd at the metal site can be summarized as follows. The hydrogen bond reflected in $^{h3}J_{NC'}$ for C39→A44 is strong and extremely stable as a function of temperature as opposed to the equivalent hydrogen bond in CpRd, which shows a tendency to a 10−20% decrease in the temperature range 10−40 °C. This enhanced stability is complemented by the additional NH$_{44}$···S(Cys)$_{42}$ hydrogen bond, whose presence is suggested only in the thermostable protein. The role of the hydrogen bond K7→E48 might also be nonnegligible in this stabilization process as it locks the remote end of the second loop to the first metal binding loop. This additional interaction and the G45P substitution in PfRd might rigidify segment 44−49 of the protein and thus prevent solvent accessibility to the metal. The hydrogen bonds of the β-sheet appear to be the keepers of an energetic trade between the two sites, and any modification in their surroundings or in their hydrogen-bonding partners is proposed to have a drastic effect on the stability of the metal binding site (Figure 6).

The complexity of the above explanation may be less than satisfying. However, one must realize that the enhanced thermal stability does not require a large ΔH or ΔS contribution, and it may be inherently hard to pinpoint the origin of such contributions. The intricate interplay of changes in hydrogen bonding seen here points to the difficulty in localizing effects. We must also be cognizant of the fact that the origin does not have to be solely in the stabilization of the native folded state but could be partly in the destabilization of the denatured state. The latter changes could be particularly difficult to assess. There have been some advances in an ability to characterize denatured, or partially denatured, states by NMR (for a review see refs *96* and *97*), but these characterizations fall short of any quantitative energetic analysis.

To date, stability studies on rubredoxin chimera exhibiting lower stability when a partial mesophile β-sheet is added to a hyperthermophile sequence support the present explanation; nevertheless, building a more stable chimera from a mesophile sequence, by substituting the hyperthermophile β-sheet (residues 3−7, 11−13, 48−52) and metal site (residues 6−11, 39−44), may offer more conclusive evidence. Extension of the present studies to the corresponding Cp, Pf, or chimera aporubredoxins may also be of particular interest. First, it has the potential to provide a rationale for the impact of the stabilization brought by the metal in the folded state of the proteins. Second, monitoring of the hydrogen bond network as a function of temperature may shed light on the previously observed difference in temperature behavior of Cp and Pf aporubredoxins (*28*). In elucidating the origin of differences between metal-containing and apo forms, advantage could be taken of a structural comparison between the native apoproteins and Cys mutants engineered as suggested by Strop and Mayo (*94*).

ACKNOWLEDGMENT

The authors acknowledge Dr. John Glushka (CCRC, University of Georgia) for help in technical support and Dr. Kumar Kolli (CCRC, University of Georgia) for the collection of electrospray ionization mass spectra.

SUPPORTING INFORMATION AVAILABLE

Tables of acquisition and processing parameters of NMR experiments used for the assignment of Cp and Pf rubredoxins, of ^{1}H, ^{13}C, and ^{15}N chemical shift assignments for fMet-CpRdZn and fMet-PfRdZn at 25 °C, of $^{1}J_{\mathrm{NH}}$, $^{1}J_{\mathrm{NC'}}$, $^{2}J_{\mathrm{NC'}}$, and $^{3}J_{\mathrm{NC'}}$ scalar couplings measured for fMet-CpRdZn and fMet-PfRdZn at 25 °C, of $^{2}J_{\mathrm{NC'}}$, $^{3}J_{\mathrm{NC'}}$, and $^{\mathrm{h3}}J_{\mathrm{NC'}}$ scalar couplings measured for fMet-CpRdZn and fMet-PfRdZn at different temperatures, and of ^{1}H, ^{15}N, and ^{13}C chemical shift temperature gradients; also, a comparison of X-ray and NMR parameters related to all of the hydrogen bonds deduced from the analysis of crystal structures available for Cp and Pf (Table S8). This material is available free of charge via the Internet at http://pubs.acs.org.

REFERENCES

1. Vieille, C., and Zeikus, G. J. (2001) Hyperthermophilic enzymes: Sources, uses, and molecular mechanisms for thermostability, *Microbiol. Mol. Biol. Rev. 65*, 1−43.
2. Sterner, R., and Liebl, W. (2001) Thermophilic adaptation of proteins, *Crit. Rev. Biochem. Mol. Biol. 36*, 39−106.
3. Szilagyi, A., and Zavodszky, P. (2000) Structural differences between mesophilic, moderately thermophilic and extremely thermophilic protein subunits: results of a comprehensive survey, *Struct. Folding Des. 8*, 493−504.
4. Kumar, S., Tsai, C. J., and Nussinov, R. (2000) Factors enhancing protein thermostability, *Protein Eng. 13*, 179−191.
5. Vogt, G., Woell, S., and Argos, P. (1997) Protein thermal stability, hydrogen bonds, and ion pairs, *J. Mol. Biol. 269*, 631−643.
6. Jenney, F. E., and Adams, M. W. W. (2001) Rubredoxin from *Pyrococcus furiosus*, *Methods Enzymol. 334*, 45−55.
7. Fiala, G., and Stetter, K. O. (1986) *Pyrococcus furiosus* represents a novel genus of marine heterotrophic archaebacteria growing optimally at 100 degrees C, *Arch. Microbiol. 145*, 56−61.
8. Blake, P. R., Park, J. B., Bryant, F. O., Aono, S., Magnuson, J. K., Eccleston, E., Howard, J. B., Summers, M. F., and Adams, M. W. W. (1991) Determinants of protein hyperthermostability − Purification and amino-acid-sequence of rubredoxin from the hyperthermophilic archaebacterium *Pyrococcus furiosus* and secondary structure of the zinc adduct by NMR, *Biochemistry 30*, 10885−10895.
9. Frey, M., Sieker, L., Payan, F., Haser, R., Bruschi, M., Pepe, G., and Legall, J. (1987) Rubredoxin from *Desulfovibrio gigas* − a molecular model of the oxidized form at 1.4 Å resolution, *J. Mol. Biol. 197*, 525−541.
10. Dauter, Z., Sieker, L. C., and Wilson, K. S. (1992) Refinement of rubredoxin from *Desulfovibrio vulgaris* at 1.0 Å with and without restraints, *Acta Crystallogr., Sect. B: Struct. Commun. 48*, 42−59.
11. Watenpaugh, K. D., Sieker, L. C., and Jensen, L. H. (1980) Crystallographic refinement of rubredoxin at 1.2 Å resolution, *J. Mol. Biol. 138*, 615−633.
12. *Desulfovibrio desulfuricans* rubredoxin was omitted due to its shorter amino acid sequence (45 instead of 53−54 residues).
13. Cavagnero, S., Zhou, Z. H., Adams, M. W. W., and Chan, S. I. (1995) Response of rubredoxin from *Pyrococcus furiosus* to environmental changes − Implications for the origin of hyperthermostability, *Biochemistry 34*, 9865−9873.
14. Papavassiliou, P., and Hatchikian, E. C. (1985) Isolation and characterization of a rubredoxin and a 2-(4Fe-4S) Ferredoxin from *Thermodesulfobacterium commune, Biochim. Biophys. Acta 810*, 1−11.
15. Eidsness, M. K., Richie, K. A., Burden, A. E., Kurtz, D. M., and Scott, R. A. (1997) Dissecting contributions to the thermostability of *Pyrococcus furiosus* rubredoxin: beta-sheet chimeras, *Biochemistry 36*, 10406−10413.
16. Cavagnero, S., Debe, D. A., Zhou, Z. H., Adams, M. W. W., and Chan, S. I. (1998) Kinetic role of electrostatic interactions in the unfolding of hyperthermophilic and mesophilic rubredoxins, *Biochemistry 37*, 3369−3376.
17. Hiller, R., Zhou, Z. H., Adams, M. W. W., and Englander, S. W. (1997) Stability and dynamics in a hyperthermophilic protein with melting temperature close to 200 degrees C, *Proc. Natl. Acad. Sci. U.S.A. 94*, 11329−11332.
18. Bonomi, F., Fessas, D., Iametti, S., Kurtz, D. M., and Mazzini, S. (2000) Thermal stability of *Clostridium pasteurianum* rubredoxin: Deconvoluting the contributions of the metal site and the protein, *Protein Sci. 9*, 2413−2426.
19. Cavagnero, S., Zhou, Z. H., Adams, M. W. W., and Chan, S. I. (1998) Unfolding mechanism of rubredoxin from *Pyrococcus furiosus*, *Biochemistry 37*, 3377−3385.
20. Day, M. W., Hsu, B. T., Joshuator, L., Park, J. B., Zhou, Z. H., Adams, M. W. W., and Rees, D. C. (1992) X-ray crystal-structures of the oxidized and reduced forms of the rubredoxin from the marine hyperthermophilic archaebacterium *Pyrococcus furiosus*, *Protein Sci. 1*, 1494−1507.
21. Blake, P. R., Park, J. B., Adams, M. W. W., and Summers, M. F. (1992) Novel observation of NH···S(Cys) hydrogen-bond-mediated scalar coupling in Cd-113-substituted rubredoxin from *Pyrococcus furiosus*, *J. Am. Chem. Soc. 114*, 4931−4933.
22. Blake, P. R., Lee, B., Summers, M. F., Adams, M. W. W., Park, J. B., Zhou, Z. H., and Bax, A. (1992) Quantitative measurement of small through-hydrogen-bond and through-space H-1-Cd-113 and H-1-Hg-199 J-couplings in metal-substituted rubredoxin from *Pyrococcus furiosus*, *J. Biomol. NMR 2*, 527−533.
23. Ayhan, M., Xiao, Z. G., Lavery, M. J., Hamer, A. M., Nugent, K. W., Scrofani, S. D. B., Guss, M., and Wedd, A. G. (1996) The rubredoxin from *Clostridium pasteurianum*: Mutation of the conserved glycine residues 10 and 43 to alanine and valine, *Inorg. Chem. 35*, 5902−5911.
24. Blake, P. R., Lee, B., Summers, M. F., Park, J. B., Zhi, H. Z., and Adams, M. W. W. (1994) Heteronuclear Magnetic-Resonance Studies of Zn, Cd-113, and Hg-199 substituted *P. furiosus* rubredoxin − Implications for biological electron-transfer, *New J. Chem. 18*, 387−395.
25. Xiao, Z. G., Maher, M. J., Cross, M., Bond, C. S., Guss, J. M., and Wedd, A. G. (2000) Mutation of the surface valine residues 8 and 44 in the rubredoxin from *Clostridium pasteurianum*: solvent access versus structural changes as determinants of reversible potential, *J. Biol. Inorg. Chem. 5*, 75−84.
26. Eidsness, M. K., Burden, A. E., Richie, K. A., Kurtz, D. M., Scott, R. A., Smith, E. T., Ichiye, T., Beard, B., Min, T. P., and Kang, C. H. (1999) Modulation of the redox potential of the [Fe(SCys)-(4)] site in rubredoxin by the orientation of a peptide dipole, *Biochemistry 38*, 14803−14809.
27. Strop, P., and Mayo, S. L. (2000) Contribution of surface salt bridges to protein stability, *Biochemistry 39*, 1251−1255.
28. Zartler, E. R., Jenney, F. E., Terrell, M., Eidsness, M. K., Adams, M. W. W., and Prestegard, J. H. (2001) Structural basis for thermostability in aporubredoxins from *Pyrococcus furiosus* and *Clostridium pasteurianum*, *Biochemistry 40*, 7279−7290.

29. Bradley, E. A., Stewart, D. E., Adams, M. W. W., and Wampler, J. E. (1993) Investigations of the thermostability of rubredoxin models using molecular-dynamics simulations, *Protein Sci. 2*, 650−665.
30. Jung, D. H., Kang, N. S., and Jhon, M. S. (1997) Site-directed mutation study on hyperthermostability of rubredoxin from *Pyrococcus furiosus* using molecular dynamics simulations in solution, *J. Phys. Chem. A 101*, 466−471.
31. Blake, P. R., Day, M. W., Hsu, B. T., Joshuator, L., Park, J. B., Hare, D. R., Adams, M. W. W., Rees, D. C., and Summers, M. F. (1992) Comparison of the X-ray structure of native rubredoxin from *Pyrococcus furiosus* with the NMR structure of the zinc-substituted protein, *Protein Sci. 1*, 1522−1525.
32. Bau, R., Rees, D. C., Kurtz, D. M., Scott, R. A., Huang, H. S., Adams, M. W. W., and Eidsness, M. K. (1998) Crystal structure of rubredoxin from *Pyrococcus furiosus* at 0.95 angstrom resolution, and the structures of N-terminal methionine and formylmethionine variants of PfRd. Contributions of N-terminal interactions to thermostability, *J. Biol. Inorg. Chem. 3*, 484−493.
33. Richie, K. A., Teng, Q., Elkin, C. J., and Kurtz, D. M. (1996) 2D H-1 and 3D H-1-N-15 NMR of zinc-rubredoxins: Contributions of the beta-sheet to thermostability, *Protein Sci. 5*, 883−894.
34. Dingley, A. J., Cordier, F., and Grzesiek, S. (2001) An introduction to hydrogen bond scalar coupling, *Concepts Magn. Reson. 13*, 103−127.
35. Grzesiek, S., Cordier, F., and Dingley, A. J. (2001) Scalar couplings across hydrogen bonds, *Methods Enzymol. 338*, 111−133.
36. Cordier, F., and Grzesiek, S. (1999) Direct observation of hydrogen bonds in proteins by interresidue $^{3h}J_{NC'}$ scalar couplings, *J. Am. Chem. Soc. 121*, 1601−1602.
37. Cornilescu, G., Hu, J.-S., and Bax, A. (1999) Identification of the hydrogen bonding network in a protein by scalar couplings, *J. Am. Chem. Soc. 121*, 2949−2950.
38. Wang, Y.-X., Jacob, J., Cordier, F., Wingfield, P., Stahl, S. J., Lee-Huang, S., Torchia, D., Grzesiek, S., and Bax, A. (1999) Measurement of $^{3h}J_{NC'}$ connectivities across hydrogen bonds in a 30 kDa protein, *J. Biomol. NMR 14*, 181−184.
39. Meissner, A., and Sørensen, O. W. (2000) New techniques for the measurement of C′−N and C ′H−N J coupling constants across hydrogen bonds in proteins, *J. Magn. Reson. 143*, 387−390.
40. Liu, A., Hu, W. D., Qamar, S., and Majumdar, A. (2000) Sensitivity enhanced NMR spectroscopy by quenching scalar coupling mediated relaxation: Application to the direct observation of hydrogen bonds in C-13/N-15-labeled proteins, *J. Biomol. NMR 17*, 55−61.
41. Liu, A. Z., Hu, W. D., Majumdar, A., Rosen, M. K., and Patel, D. J. (2000) Detection of very weak side chain-main chain hydrogen bonding interactions in medium-size C-13/N-15-labeled proteins by sensitivity-enhanced NMR spectroscopy, *J. Biomol. NMR 17*, 79−82.
42. Cornilescu, G., Ramirez, B. E., Frank, K. M., Clore, M. G., Gronenborn, A. M., and Bax, A. (1999) Correlation between $^{3h}J_{NC'}$ and hydrogen bond length in proteins, *J. Am. Chem. Soc. 121*, 6275−6279.
43. Liu, A. Z., Hu, W. D., Majumdar, A., Rosen, M. K., and Patel, D. J. (2000) NMR detection of side chain-side chain hydrogen bonding interactions in C-13/N-15-labeled proteins, *J. Biomol. NMR 17*, 305−310.
44. Hennig, M., and Geierstanger, B. H. (1999) Direct detection of a histidine-histidine side chain hydrogen bond important for folding of apomyoglobin, *J. Am. Chem. Soc. 121*, 5123−5126.
45. Alexandrescu, A. T., Snyder, D. R., and Abildgaard, F. (2001) NMR of hydrogen bonding in cold-shock protein A and an analysis of the influence of crystallographic resolution on comparisons of hydrogen bond lengths, *Protein Sci. 10*, 1856−1868.
46. Scheurer, C., and Bruschweiler, R. (1999) Quantum-chemical characterization of nuclear spin−spin couplings across hydrogen bonds, *J. Am. Chem. Soc. 121*, 8661−8662.
47. Pecul, M., Leszczynski, J., and Sadlej, J. (2000) The shielding constants and scalar couplings in N−H···O═C and N−H···N═C hydrogen bonded systems: An ab initio MO study, *J. Phys. Chem. A 104*, 8105−8113.
48. Arnold, W. D., and Oldfield, E. (2000) The chemical nature of hydrogen bonding in proteins via NMR: J-couplings, chemical shifts, and AIM theory, *J. Am. Chem. Soc. 122*, 12835−12841.
49. Bagno, A. (2000) Quantum chemical modeling of through-hydrogen bond spin−spin coupling in amides and ubiquitin, *Chem.−Eur. J. 6*, 2925−2930.
50. Barfield, M. (2002) Structural dependencies of interresidue scalar coupling (h3)J(NC), and donor H-1 chemical shifts in the hydrogen bonding regions of proteins, *J. Am. Chem. Soc. 124*, 4158−4168.
51. Cordier, F., and Grzesiek, S. (2002) Temperature-dependence properties as studied by of protein hydrogen bond high-resolution NMR, *J. Mol. Biol. 317*, 739−752.
52. Li, H., Yamada, H., Akasaka, K., and Gronenborn, A. M. (2000) Pressure alters electronic orbital overlap in hydrogen bonds, *J. Biomol. NMR 18*, 207−216.
53. Cordier, F., Wang, C. Y., Grzesiek, S., and Nicholson, L. K. (2000) Ligand-induced strain in hydrogen bonds of the c-Src-SH3 domain detected by NMR, *J. Mol. Biol. 304*, 497−505.
54. Jaravine, V. A., Alexandrescu, A. T., and Grzesiek, S. (2001) Observation of the closing of individual hydrogen bonds during TFE-induced helix formation in a peptide, *Protein Sci. 10*, 943−950.
55. Chemical shifts are for the most part insensitive to pH changes between 6 and 8.
56. Calculated molecular weights for 100% [U-^{15}N,^{13}C]-fMet-CpRdZn, CpRdZn, fMet-PfRdZn, Met-PfRdZn, and wt-PfRdZn are respectively 6461.59, 6432.58, 6443.68, 6414.67, and 6277.52 g·mol^{-1}. Electrospray ionization mass spectra were collected on a Micromass Q-Tof-II spectrometer, after sample desalting. Experimental molecular weights agree, within 0.03%, with the Rd masses predicted for the fully labeled demetalated species.
57. Kay, L. E., Keifer, P., and Saarinen, T. (1992) Pure absorption gradient enhanced heteronuclear single quantum correlation spectroscopy with improved sensitivity, *J. Am. Chem. Soc. 114*, 10663−10665.
58. Kay, L. E., Xu, G. Y., and Yamazaki, T. (1994) Enhanced-sensitivity triple-resonance spectroscopy with minimal H_2O saturation, *J. Magn. Reson., Ser. A 109*, 129−133.
59. Grzesiek, S., and Bax, A. (1993) The origin and removal of artifacts in 3D-HCACO spectra of proteins uniformly enriched with C-13, *J. Magn. Reson., Ser. B 102*, 103−106.
60. Olejniczak, E. T., and Fesik, S. W. (1994) 2-Dimensional nuclear-magnetic-resonance method for identifying the H-alpha/C-alpha signals of amino acid-residues preceding proline, *J. Am. Chem. Soc. 116*, 2215−2216.
61. Marion, D., Ikura, M., Tschudin, R., and Bax, A. (1989) Rapid recording of 2D NMR-spectra without phase cycling − Application to the study of hydrogen-exchange in proteins, *J. Magn. Reson. 85*, 393−399.
62. Schleucher, J., Sattler, M., and Griesinger, C. (1993) Coherence selection by gradients without signal attenuation − Application to the 3-Dimensional HNCO experiment, *Angew. Chem., Int. Ed. Engl. 32*, 1489−1491.
63. Kay, L. E., Xu, G. Y., Singer, A. U., Muhandiram, D. R., and Formankay, J. D. (1993) A gradient-enhanced HCCH-TOCSY experiment for recording side-chain H-1 and C-13 correlations in H_2O samples of proteins, *J. Magn. Reson., Ser. B 101*, 333−337.
64. Yamazaki, T., Formankay, J. D., and Kay, L. E. (1993) 2-Dimensional NMR experiments for correlating C-13-beta and H-1-delta/epsilon chemical-shifts of aromatic residues in C-13-labeled proteins via scalar couplings, *J. Am. Chem. Soc. 115*, 11054−11055.
65. Muhandiram, D. R., Farrow, N. A., Xu, G. Y., Smallcombe, S. H., and Kay, L. E. (1993) A gradient C-13 NOESY-HSQC experiment for recording NOESY spectra of C-13-labeled proteins dissolved in H_2O, *J. Magn. Reson., Ser. B 102*, 317−321.
66. Löhr, F., and Rüterjans, H. (1996) Novel pulse sequences for the resonance assignment of aromatic side chains in C-13-labeled proteins, *J. Magn. Reson., Ser. B 112*, 259−268.
67. Yamazaki, T., Yoshida, M., and Nagayama, K. (1993) Complete assignments of magnetic resonances of Ribonuclease-H from *Escherichia coli* by double-resonance and triple-resonance 2D and 3D NMR spectroscopies, *Biochemistry 32*, 5656−5669.
68. Wishart, D. S., Bigam, C. G., Yao, J., Abildgaard, F., Dyson, H. J., Oldfield, E., Markley, J. L., and Sykes, B. D. (1995) H-1, C-13 and N-15 chemical-shift referencing in biomolecular NMR, *J. Biomol. NMR 6*, 135−140.
69. Reported assignments refer to the major species present in the CpRdZn and PfRdZn samples, i.e., the fMet forms in both cases. Backbone-only assignments are reported for MetCpRdZn and do not significantly differ from the fMet form. Specific backbone assignments could not be pursued for the wt-PfRdZn and Met-PfRdZn species due to their lower percentage in the sample and resonance overlap with the major fMet-PfRdZn component.

70. Cavanagh, J., Fairbrother, W. J., Palmer, A. G., III, and Skelton, N. J. (1996) *Protein NMR spectroscopy Principles and Practice*, Academic Press, San Diego.
71. Schwarzinger, S., Kroon, G. J. A., Foss, T. R., Wright, P. E., and Dyson, H. J. (2000) Random coil chemical shifts in acidic 8 M urea: Implementation of random coil shift data in NMRView, *J. Biomol. NMR 18*, 43−48.
72. Schwarzinger, S., Kroon, G. J. A., Foss, T. R., Chung, J., Wright, P. E., and Dyson, H. J. (2001) Sequence-dependent correction of random coil NMR chemical shifts, *J. Am. Chem. Soc. 123*, 2970−2978.
73. Case, D. A. (1995) Calibration of ring-current effects in proteins and nucleic acids, *J. Biomol. NMR 6*, 341−346.
74. No significant difference in the ring current shifts was noted when lower resolution structures were used.
75. Bodenhausen, G., and Ruben, D. J. (1980) Natural abundance N-15 NMR by enhanced heteronuclear spectroscopy, *Chem. Phys. Lett. 69*, 185−189.
76. Ottiger, M., Delaglio, F., and Bax, A. (1998) Measurement of J and dipolar couplings from simplified two-dimensional NMR spectra, *J. Magn. Reson. 131*, 373−378.
77. Tolman, J. R., and Prestegard, J. H. (1996) A quantitative J-correlation experiment for the accurate measurement of one-bond amide N-15-H-1 couplings in proteins, *J. Magn. Reson., Ser. B 112*, 245−252.
78. Prantner, A. M., Volkman, B. F., Wilkens, S. J., Xia, B., and Markley, J. L. (1997) Assignment of 1H, 13C and 15N signals of reduced *Clostridium pasteurianum* rubredoxin: Oxidation state-dependent changes in chemical shifts and relaxation rates, *J. Biomol. NMR 10*, 411−412.
79. Bertini, I., Kurtz, D. M., Eidsness, M. K., Liu, G., Luchinat, C., Antonio, R., and Scott, R. A. (1998) Solution structure of reduced *Clostridium pasteurianum* rubredoxin, *J. Biol. Inorg. Chem. 3*, 401−410.
80. Volkman, B. F., Prantner, A. M., Wilkens, S. J., Xia, B., and Markley, J. L. (1997) Assignment of ^{1}H, ^{13}C and ^{15}N signals of oxidized *Clostridium pasteurianum* rubredoxin, *J. Biomol. NMR 10*, 409−410.
81. Blake, P. R., Park, J. B., Zhou, Z. H., Hare, D. R., Adams, M. W. W., and Summers, M. F. (1992) Solution-State Structure by NMR of zinc-substituted rubredoxin from the marine hyperthermophilic archaebacterium *Pyrococcus furiosus*, *Protein Sci. 1*, 1508−1521.
82. Dijkstra, K., Kroon, G. J. A., Vannuland, N. A. J., and Scheek, R. M. (1994) The COCAH experiment to correlate intraresidue Carbonyl, C-alpha, and H-alpha resonances in proteins, *J. Magn. Reson., Ser. A 107*, 102−105.
83. Huang, C. C., Couch, G. S., Pettersen, E. F., and Ferrin, T. E. (1996) Chimera: An extensible molecular modeling application constructed using standard components, *Pac. Symp. Biocomput. 1*, 724.
84. Hernandez, G., and LeMaster, D. M. (2001) Reduced temperature dependence of collective conformational opening in a hyperthermophile rubredoxin, *Biochemistry 40*, 14384−14391.
85. Del Bene, J. E., Perera, S. A., and Bartlett, R. J. (2000) Predicted NMR coupling constants across hydrogen bonds: A fingerprint for specifying hydrogen bond type?, *J. Am. Chem. Soc. 122*, 3560−3561.
86. Wagner, G., Pardi, A., and Wuthrich, K. (1983) Hydrogen-bond length and H-1-NMR chemical-shifts in proteins, *J. Am. Chem. Soc. 105*, 5948−5949.
87. Tessari, M., Vis, H., Boelens, R., Kaptein, R., and Vuister, G. W. (1997) Quantitative measurement of relaxation interference effects between H-1(N)-CSA and H-1-N-15 dipolar interaction: Correlation with secondary structure, *J. Am. Chem. Soc. 119*, 8985−8990.
88. Tjandra, N., and Bax, A. (1997) Solution NMR measurement of amide proton chemical shift anisotropy in N-15-enriched proteins. Correlation with hydrogen bond length, *J. Am. Chem. Soc. 119*, 8076−8082.
89. Juranic, N., Ilich, P. K., and Macura, S. (1995) Hydrogen-bonding networks in proteins as revealed by the amide $^{1}J_{NC'}$ coupling-constant, *J. Am. Chem. Soc. 117*, 405−410.
90. Juranic, N., and Macura, S. (2001) Correlations among $^{1}J_{NC'}$ and $^{h3}J_{NC'}$ coupling constants in the hydrogen-bonding network of human ubiquitin, *J. Am. Chem. Soc. 123*, 4099−4100.
91. Andersen, N. H., Neidigh, J. W., Harris, S. M., Lee, G. M., Liu, Z. H., and Tong, H. (1997) Extracting information from the temperature gradients of polypeptide NH chemical shifts. 1. The importance of conformational averaging, *J. Am. Chem. Soc. 119*, 8547−8561.
92. Walling, A. E., Pargas, R. E., and deDios, A. C. (1997) Chemical shift tensors in peptides: A quantum mechanical study, *J. Phys. Chem. A 101*, 7299−7303.
93. Bonomi, F., Burden, A. E., Eidsness, M. K., Fessas, D., Iametti, S., Kurtz, D. M., Mazzini, S., Scott, R. A., and Zeng, Q. D. (2002) Thermal stability of the [Fe(SCys)(4)] site in *Clostridium pasteurianum* rubredoxin: contributions of the local environment and Cys ligand protonation, *J. Biol. Inorg. Chem. 7*, 427−436.
94. Strop, P., and Mayo, S. L. (1999) Rubredoxin variant folds without iron, *J. Am. Chem. Soc. 121*, 2341−2345.
95. Koradi, R., Billeter, M., and Wuthrich, K. (1996) MolMol: a program for display and analysis of macromolecular structures, *J. Mol. Graphics 14*, 51−55.
96. Dyson, H. J., and Wright, P. E. (1996) Insights into protein folding from NMR, *Annu. Rev. Phys. Chem. 47*, 369−395.
97. Van Nuland, N. A. J., Forge V., Balbach J., and Dobson C. M. (1998) Real-time NMR studies of protein folding, *Acc. Chem. Res. 31*, 773−780.

BI027264D